On Discrete-Time/Frequency-Periodic End-to-End Fiber-Optical Channel Models

Felix Frey, Johannes K. Fischer, *Senior Member, IEEE,* and Robert F.H. Fischer, *Senior Member, IEEE*

arXiv:1907.06087v1 [eess.SP] 13 Jul 2019

***Abstract*—A discrete-time end-to-end fiber-optical channel model is derived based on the first-order perturbation approach. The model relates the discrete-time input symbol sequences of co-propagating wavelength channels to the received symbol sequence after matched filtering and T-spaced sampling. To that end, the interference from both self- and cross-channel nonlinear interactions of the continuous-time *optical* signal is represented by a single discrete-time perturbative term. Two equivalent models can be formulated—one in the discrete-time domain, the other in the $1/T$-periodic continuous-frequency domain. The time-domain formulation coincides with the *pulse-collision picture* and its correspondence to the frequency-domain description is derived. The latter gives rise to a novel perspective on the end-to-end input/output relation of optical transmission systems. Both views can be extended from a regular, i.e., solely additive model, to a combined regular-logarithmic model to take the multiplicative nature of certain degenerate distortions into consideration. We provide an alternative formulation of the *Gaussian Noise* model and derive a novel algorithm for application in low-complexity fiber nonlinearity compensation. The derived end-to-end model requires only a single computational step and shows good agreement in the mean-squared error sense compared to the oversampled and inherently sequential split-step Fourier method.**

***Index Terms*—Fiber nonlinear optics, channel models, nonlinear signal-signal interaction.**

I. Introduction

In communication theory, discrete-time end-to-end channel models play a fundamental role in developing advanced transmission and equalization schemes. Most notable the discrete-time *linear*, dispersive channel with additive white Gaussian noise (AWGN) is often used to model *point-to-point* transmission scenarios. In the last decades, a large number of transmission methods for such linear channels have emerged and are now applied in many standards in the field of digital transmission systems. With the advent of high-speed CMOS technology, those schemes have also been adopted in applications for *fiber-optical* transmission with digital-coherent reception [1]. However, many of the applied techniques (e.g., coded modulation, signal shaping, and equalization) are designed for linear channels whereas the fiber-optical channel is inherently *nonlinear*. An exact model to obtain the output sequence from a given input sequence by an *explicit* input/output relation is highly desirable to make further advances in developing strategies optimized for fiber-optical transmission. In analogy to the continuous-time AWGN channel being reduced to a discrete-time channel, the respective formulation for the fiber-optical channel may allow for a new class of transmission schemes optimized to the particular conditions faced during nonlinear transmission.

Indeed, many works in the past two decades were devoted to develop channel models for fiber-optic transmission with good trade-offs between computational complexity and numerical accuracy. Starting from the nonlinear Schrödinger equation (NLSE), approximate solutions can be obtained following either a *perturbative approach* (cf. [2, P. 610]) or the equivalent method of Volterra series transfer function (VSTF) (cf. [3], [4]). These channel models can approximate the nonlinear distortion—there commonly termed nonlinear interference (NLI)—up to the order of the series expansion of the NLSE. A comprehensive summary of recent developments on channel models can be found in [5, Sec. I].

One particular class of channel models—based on a first-order time-domain perturbative approach—has been published in the early 2000s in a series of contributions by Antonio Mecozzi in collaboration with a group from AT&T Labs [6]–[8]. The results, however, were limited to transmission schemes that were practical at that time (e.g., dispersion-managed transmission, intensity-modulation and direct-detection). The details of the theory and its derivation were published recently in [9]. A follow-up seminal paper with René-Jean Essiambre [10] extents the former work by including the *matched filter* and T-spaced sampling after ideal coherent detection. One central result of this work is the integral formulation of the (Volterra or perturbation) *kernel coefficients* providing a first-order approximation of the *per-modulation-interval* T equivalent end-to-end input/output relation. Based on this work the joint contributions with Ronen Dar and colleagues [11]–[13] resulted in the so-called *pulse-collision picture* of the nonlinear fiber-optical channel. Here, the properties of cross-channel NLI were properly associated with certain types of pulse collisions in *time*-domain.

In this contribution, we aim to complement the view on T-spaced end-to-end channel models for optical transmission systems by an equivalent *frequency*-domain description. We provide an integral solution which relates the periodic spectrum of the transmit sequence to the periodic spectrum of the receive sequence, i.e., after (linear) channel matched filtering and aliasing to frequencies within the Nyquist interval. The time discretization with symbol spacing T translates to a $1/T$-periodic representation in frequency. Remarkably, the *frequency-matching* which is imposed along with the general

F. Frey and R. F.H. Fischer are with the Institute of Communications Engineering, Ulm University, 89081 Ulm, Germany (e-mail: {felix.frey, robert.fischer} @uni-ulm.de)

J.K. Fischer is with the Photonics Networks and Systems department at Fraunhofer Heinrich-Hertz-Institute, Einsteinufer 37, 10587 Berlin, Germany.

Funded by the Deutsche Forschungsgemeinschaft (DFG, German Research Foundation)—grant FI 982/14-1.

four wave mixing (FWM) process in the optical domain is still maintained in the periodic frequency-domain.

The structure of this paper is organized as follows. In Section II, the notation is briefly introduced and the system model of coherent fiber-optical transmission is presented. In Section III, starting from the *continuous-time* end-to-end relation of the *optical* channel—an intermediate result following the perturbation approach—the *discrete-time* end-to-end relation is derived. We particularly highlight the relation between the time and frequency representation and point out the connection to other well-known channel models. The relevant system parameters, i.e., *memory* and *strength*, of the nonlinear response are identified which lead to design rules of practical schemes for fiber nonlinearity mitigation. For such schemes, a novel algorithm in a $1/T$-periodic frequency-domain is introduced well-suited also for systems operating at very high symbol rates. Similar to the pulse-collision picture, certain degenerate mixing products in frequency-domain can be attributed to a pure phase and polarization rotation. This in turn motivates the extension of the original *regular* perturbation model to a combined *regular-logarithmic* model taking the multiplicative nature of certain distortions properly into account. In Section IV, the theoretical considerations are complemented by numerical simulations which are in accordance with results obtained by the split-step Fourier method (SSFM). Here, the relevant metric to assess the match between both models is the mean-squared error (MSE) between the two T-spaced output sequences for a given input sequence. Section V presents some conclusions.

II. Notation and System Model

This section briefly introduces the notation and the overall system model to make this contribution as self-contained as possible.

A. Notation and Basic Definitions

Sets are denoted with calligraphic letters, e.g., $\mathcal{A}$ is the set of data symbols, i.e., the symbol *alphabet* or *signal constellation*. A *set of numbers* or *finite fields* are typeset in blackboard bold typeface, e.g., the set of real numbers is $\mathbb{R}$. Bold letters, such as $\boldsymbol{x}$, indicate vectors. If not stated otherwise, a vector $\boldsymbol{x} = [x_1, x_2, \ldots, x_n]^{\mathsf{T}}$ of dimension n is a column vector[1], and the set of indices to the elements of the vector is $\mathcal{I} \stackrel{\text{def}}{=} \{1, \ldots, n\}$. Non-bold italic letters, like x, are scalar variables, whereas non-bold Roman letters refer to constants, e.g., the imaginary number is j with $\mathrm{j}^2 = -1$.

A *real* (bandpass) signal is typically described using the equivalent complex baseband (ECB) representation, i.e., we consider the complex envelope $x(t) \in \mathbb{C}$ with *inphase* (real) and *quadrature* (imaginary) component.

The n-dimensional *Fourier transform* of a continuous-time signal $x(\boldsymbol{t}) = x(t_1, t_2, \ldots, t_n)$ depending on the n-dimensional time vector $\boldsymbol{t} = [t_1, t_2, \ldots, t_n]^{\mathsf{T}} \in \mathbb{R}^n$ (in *seconds*) is denoted by $X(\boldsymbol{\omega}) = \mathcal{F}\{\, x(\boldsymbol{t}) \,\}$, and defined as [14, Ch. 4]

$$X(\boldsymbol{\omega}) = \mathcal{F}\{\, x(\boldsymbol{t}) \,\} \stackrel{\text{def}}{=} \int_{\mathbb{R}^n} x(\boldsymbol{t})\, \mathrm{e}^{-\mathrm{j}\boldsymbol{\omega}\cdot\boldsymbol{t}}\, \mathrm{d}^n\boldsymbol{t} \tag{1}$$

$$x(\boldsymbol{t}) = \mathcal{F}^{-1}\{\, X(\boldsymbol{\omega}) \,\} = \frac{1}{(2\pi)^n} \int_{\mathbb{R}^n} X(\boldsymbol{\omega})\, \mathrm{e}^{\mathrm{j}\boldsymbol{\omega}\cdot\boldsymbol{t}}\, \mathrm{d}^n\boldsymbol{\omega}. \tag{2}$$

Here, $X(\boldsymbol{\omega})$ is a continuous function of *angular frequencies* $\boldsymbol{\omega} = [\omega_1, \omega_2, \ldots, \omega_n]^{\mathsf{T}} \in \mathbb{R}^n$ with $\omega = 2\pi f$ and frequency $f \in \mathbb{R}$ (in *Hertz*). In the exponential we made use of the dot product of vectors in $\mathbb{R}^n$ given by $\boldsymbol{\omega} \cdot \boldsymbol{t} \stackrel{\text{def}}{=} \omega_1 t_1 + \omega_2 t_2 + \cdots + \omega_n t_n$. The integral is an n-fold multiple integral over $\mathbb{R}^n$ and the integration boundaries are at $-\infty$ and ∞ in each dimension. We use the expression $\mathrm{d}^n\boldsymbol{t}$ as shorthand for $\mathrm{d}t_1 \mathrm{d}t_2 \ldots \mathrm{d}t_n$. For the one-dimensional case with $n = 1$ the variable subscript is dropped. We may also write the correspondence as $x(t) \circ\!\!-\!\!\bullet\, X(\omega)$ for short.

The n-dimensional discrete-time Fourier transform (DTFT) of a discrete-time sequence[2] $\langle\, x[\boldsymbol{k}] \,\rangle$ with $\boldsymbol{k} = [k_1, k_2, \ldots, k_n]^{\mathsf{T}} \in \mathbb{Z}^n$ with spacing T between symbols is periodic with $1/T$ in frequency-domain and denoted as $X(\mathrm{e}^{\mathrm{j}\boldsymbol{\omega}T}) = \hat{\mathcal{F}}\{\, x[\boldsymbol{k}] \,\}$, and defined as[3]

$$X(\mathrm{e}^{\mathrm{j}\boldsymbol{\omega}T}) = \hat{\mathcal{F}}\{\, x[\boldsymbol{k}] \,\} \stackrel{\text{def}}{=} \sum_{\boldsymbol{k}\in\mathbb{Z}^n} x[\boldsymbol{k}]\, \mathrm{e}^{-\mathrm{j}\boldsymbol{\omega}\cdot\boldsymbol{k}T} \tag{3}$$

$$x[\boldsymbol{k}] = \hat{\mathcal{F}}^{-1}\{\, X(\mathrm{e}^{\mathrm{j}\boldsymbol{\omega}T}) \,\} = \left(\frac{T}{2\pi}\right)^n \int_{\mathbb{T}^n} X(\mathrm{e}^{\mathrm{j}\boldsymbol{\omega}T})\, \mathrm{e}^{\mathrm{j}\boldsymbol{\omega}\cdot\boldsymbol{k}T}\, \mathrm{d}^n\boldsymbol{\omega}. \tag{4}$$

The set of frequencies in the Nyquist interval is $\mathbb{T} \stackrel{\text{def}}{=} \{\, \omega \in \mathbb{R} \mid -\omega_{\mathrm{Nyq}} \leq \omega < \omega_{\mathrm{Nyq}} \,\}$ with the Nyquist (angular) frequency $\omega_{\mathrm{Nyq}} \stackrel{\text{def}}{=} 2\pi/(2T)$.

In the present work the so-called *engineering* notation of the Fourier transform with a negative sign in the complex exponential (in the forward, i.e., time-to-frequency, direction) is used. This has immediate consequences for the solution of the electro-magnetic wave equation (cf. *Helmholtz equation*), and therefore also for the NLSE. In the optical community, there exists no fixed convention with respect to the sign notation, e.g., some of the texts are written with the physicists' (e.g., [15, Eq. (2.2.8)] or [10]) and others with the engineering (e.g., [16], [17, Eq. (A.4)]) notation in mind. Consequently, the derivations shown here may differ marginally from some of the original sources.

Continuous-time signals are associated with meaningful physical units, e.g., the electrical field has typically units of *volts per meter* (V/m). The NLSE and the *Manakov equation* derived thereof are carried out in *Jones space* over a quantity $\boldsymbol{u}(t) = [u_{\mathsf{x}}(t), u_{\mathsf{y}}(t)]^{\mathsf{T}} \in \mathbb{C}^2$ called the *optical field envelope*. The optical field envelope has the same orientation as the associated electrical field but is normalized s.t. $\boldsymbol{u}^{\mathsf{H}}\boldsymbol{u}$ equals the instantaneous power given in *watts* (W). In this work, signals are instead generally treated as dimensionless entities as this considerably simplifies the notation when we move

[1] $(\cdot)^{\mathsf{T}}$ denotes transposition and $(\cdot)^{\mathsf{H}}$ is the Hermitian transposition.

[2] If *whole* (finite-length) sequence is treated, this is indicated by the square bracket notation, i.e., $\langle\, x[k] \,\rangle$.

[3] The notation $\sum_{\boldsymbol{k}\in\mathbb{Z}^n}$ is short for $\sum_{k_1=-\infty}^{\infty} \sum_{k_2=-\infty}^{\infty} \cdots \sum_{k_n=-\infty}^{\infty}$.

between the various signal domains (see, e.g., discussion in [18, P. 11] or [19, P. 230]). To this end, $\boldsymbol{u}^{\mathsf{H}}\boldsymbol{u}$ is re-normalized to be dimensionless. Similarly, the *nonlinearity coefficient* γ (commonly given in $\mathrm{W}^{-1}\mathrm{m}^{-1}$) is also re-normalized to have units of m^{-1}.

To distinguish a two-dimensional complex vector $\boldsymbol{u} = [u_{\mathsf{x}}, u_{\mathsf{y}}]^{\mathsf{T}} \in \mathbb{C}^2$ in Jones space from its associated three-dimensional real-valued vector in *Stokes space*, we use decorated bold letters $\vec{\boldsymbol{u}} = [u_1, u_2, u_3]^{\mathsf{T}} \in \mathbb{R}^3$. The (permuted) set of Pauli matrices is given by [20]

$$\boldsymbol{\sigma}_1 \stackrel{\text{def}}{=} \begin{bmatrix} 1 & 0 \\ 0 & -1 \end{bmatrix} \quad \boldsymbol{\sigma}_2 \stackrel{\text{def}}{=} \begin{bmatrix} 0 & 1 \\ 1 & 0 \end{bmatrix} \quad \boldsymbol{\sigma}_3 \stackrel{\text{def}}{=} \begin{bmatrix} 0 & -\mathrm{j} \\ \mathrm{j} & 0 \end{bmatrix}, \tag{5}$$

and the Pauli vector is $\vec{\boldsymbol{\sigma}} \stackrel{\text{def}}{=} [\boldsymbol{\sigma}_1, \boldsymbol{\sigma}_2, \boldsymbol{\sigma}_3]^{\mathsf{T}}$ where each vector component is a 2×2 Pauli matrix. The relation between Jones and Stokes space can then be established by the concise (symbolic) expression $\vec{\boldsymbol{u}} = \boldsymbol{u}^{\mathsf{H}}\vec{\boldsymbol{\sigma}}\boldsymbol{u}$ to denote the element-wise operation $u_i = \boldsymbol{u}^{\mathsf{H}}\boldsymbol{\sigma}_i\boldsymbol{u}$ for all Stokes vector components $i = 1, 2, 3$. The Stokes vector $\vec{\boldsymbol{u}}$ can also be expanded using the dot product with the Pauli vector to obtain the complex-valued 2×2 matrix with

$$\vec{\boldsymbol{u}} \cdot \vec{\boldsymbol{\sigma}} = u_1\boldsymbol{\sigma}_1 + u_2\boldsymbol{\sigma}_2 + u_3\boldsymbol{\sigma}_3 = \begin{bmatrix} u_{\mathsf{x}}u_{\mathsf{x}}^* - u_{\mathsf{y}}u_{\mathsf{y}}^* & 2u_{\mathsf{x}}u_{\mathsf{y}}^* \\ 2u_{\mathsf{x}}^*u_{\mathsf{y}} & u_{\mathsf{y}}u_{\mathsf{y}}^* - u_{\mathsf{x}}u_{\mathsf{x}}^* \end{bmatrix}, \tag{6}$$

which will later be used to describe the *instantaneous* polarization rotation around the Stokes vector $\vec{\boldsymbol{u}}$ using the Jones formalism. We may also use the equality [20, Eq. (3.9)]

$$\boldsymbol{u}\boldsymbol{u}^{\mathsf{H}} = \frac{1}{2}\left(\boldsymbol{u}^{\mathsf{H}}\boldsymbol{u}\,\mathbf{I} + \vec{\boldsymbol{u}} \cdot \vec{\boldsymbol{\sigma}}\right) \tag{7}$$

with the identity matrix $\mathbf{I}$ and $\|\boldsymbol{u}\|^2 = \boldsymbol{u}^{\mathsf{H}}\boldsymbol{u} = u_{\mathsf{x}}u_{\mathsf{x}}^* + u_{\mathsf{y}}u_{\mathsf{y}}^*$.

B. System Model

In this work we consider *point-to-point* coherent optical transmission over two planes of polarization in a single-mode fiber. This results in a complex-valued 2×2 multiple-input/multiple-output (MIMO) transmission which is typically used for multiplexing. One of the major constraints of today's fiber-optical transmission systems is the bandwidth of electronic devices which is orders of magnitude smaller than the available bandwidth of optical fibers. It is hence routine to use wavelength-division multiplexing (WDM), where a number of so-called *wavelength channels* are transmitted simultaneously through the same fiber. Each wavelength signal is modulated on an individual laser operated at a certain wavelength (or respectively at a certain frequency) such that neighboring signals do not share the same frequency band when transmitted jointly over the same fiber medium.

Fig. 1 shows the block diagram of a coherent optical transmission system exemplifying the digital, analog, and optical domains of a single wavelength channel. Within the bandwidth of a wavelength channel, we can consider the *optical end-to-end* 2×2 MIMO channel as frequency-flat if we neglect the effects of bandlimiting devices (e.g., switching elements in a routed network). The nonlinear property of the fiber-optical transmission medium is the source of interference within and between different wavelength channels. In the following, we will call the channel under consideration the *probe* channel, while a co-propagating wavelength channel is called *interferer*. This allows us to discriminate between self-channel interference (SCI) and cross-channel interference (XCI). In Fig. 1 the probe channel in the optical domain is denoted by a subscript ρ, whereas interferers are labeled by the channel index ν with $\nu \in \{1, 2, \ldots, N_{\mathrm{ch}} \mid \nu \neq \rho\}$. The various domains and its entities are discussed in the following.

1) Transmitter Frontend: The transmission system is fed with equiprobable source bits of the probe (and interferer) channel. The binary source generates uniform i.i.d. *information bits* $\mathfrak{q}[\kappa] \in \mathbb{F}_2$ at each discrete-time index $\kappa \in \mathbb{Z}$. $\mathbb{F}_2$ denotes the Galois field of size two and $\mathbb{Z}$ is the set of integers. The binary sequence $\langle\, \mathfrak{q}[\kappa] \,\rangle$ is partitioned into binary tuples of length R_{m}, s.t. $\mathfrak{q}[k] = [\mathfrak{q}_1[k], \ldots, \mathfrak{q}_{R_{\mathrm{m}}}[k]] \in \{0, 1\}^{R_{\mathrm{m}}}$, where $k \in \mathbb{Z}$ is the discrete-time index of the *data symbols*. Here, R_{m} is called the rate of the modulation and will be equivalent to the number of bits per transmitted data symbol, if we assume that the size of the symbol set is a power of two. Each R_{m}-tuple is associated with one of the possible data symbols $\boldsymbol{a} = [a_{\mathsf{x}}, a_{\mathsf{y}}]^{\mathsf{T}} \in \mathcal{A} \subset \mathbb{C}^2$, i.e., with one of the *constellation* points. We say that the binary R_{m}-tuples are mapped to the data symbols $\boldsymbol{a} \in \mathcal{A}$ by a bijective mapping rule $\mathcal{M} : \mathfrak{q} \mapsto \boldsymbol{a}$.

The size of the data symbol set is $M = |\mathcal{A}| = 2^{R_{\mathrm{m}}}$ and we can write the alphabet as $\mathcal{A} \stackrel{\text{def}}{=} \{\boldsymbol{a}_1, \ldots, \boldsymbol{a}_M\} \subset \mathbb{C}^2$. The symbol set has zero mean if not stated otherwise, that is $\mathrm{E}\{\,\boldsymbol{a}\,\} = \mathbf{0}$, and we deliberately normalize the variance of the symbol set to $\sigma_a^2 \stackrel{\text{def}}{=} \mathrm{E}\{\,\|\boldsymbol{a}\|^2\,\} = 1$ (the expectation is denoted by $\mathrm{E}\{\cdot\}$ and the Euclidean vector norm is $\|\cdot\|$). For reasons of readability we denote the data symbols of the interfering channels by $\boldsymbol{b}_\nu[k]$.

The discrete-time data symbols $\boldsymbol{a}[k]$ are converted to the continuous-time transmit signal $\boldsymbol{s}(t)$ by means of pulse-shaping constituting the digital-to-analog (D/A) transition, cf. Fig. 2 (a). We can express the transmit signal $\boldsymbol{s}(t) = [s_1(t), s_2(t)]^{\mathsf{T}} \in \mathbb{C}^2$ as a function of the data symbols with

$$\boldsymbol{s}(t) = T \cdot \sum_{k \in \mathbb{Z}} \boldsymbol{a}[k] h_{\mathrm{T}}(t - kT), \tag{8}$$

where $\boldsymbol{s}(t)$ is a superposition of a time-shifted (with symbol period T) basic pulse $h_{\mathrm{T}}(t)$ weighted by the data symbols. The pre-factor T is required to preserve a dimensionless signal in the continuous-time domain (cf. [18, P. 11]). We assume that the transmit pulse has $\sqrt{\text{Nyquist}}$ property, i.e., $|H_{\mathrm{T}}(\omega)|^2$ has Nyquist property with the Fourier pair $h_{\mathrm{T}}(t) \circ\!\!-\!\!\bullet H_{\mathrm{T}}(\omega)$. To keep the following derivations tractable, all wavelength channels transmit at the same *symbol rate* $R_{\mathrm{s}} \stackrel{\text{def}}{=} 1/T$ as the probe channel. The pulse energy E_{T} of the probe channel is given by [18, Eq. (2.2.22)]

$$E_{\mathrm{T}} = \int_{-\infty}^{\infty} |T \cdot h_{\mathrm{T}}(t)|^2 \mathrm{d}t = \frac{1}{2\pi} \int_{-\infty}^{\infty} |T \cdot H_{\mathrm{T}}(\omega)|^2 \mathrm{d}\omega. \tag{9}$$

The pulse energy E_{T} has the unit *seconds* due to the normalization of the signals. Using the symbol energy $E_{\mathrm{s}} \stackrel{\text{def}}{=} \sigma_a^2 E_{\mathrm{T}}$,

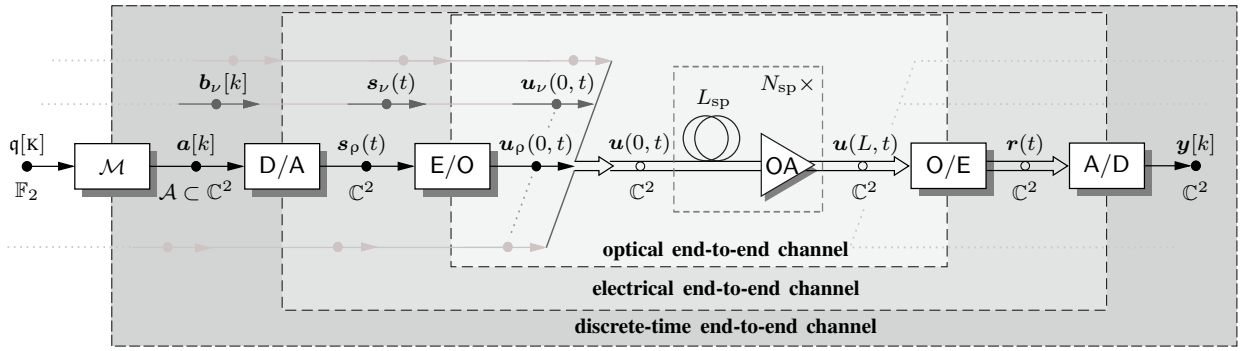

Fig. 1. Generic fiber-optical transmission system model.

the average signal power P calculates to [18, Eq. (4.1.1)]

$$P \overset{\text{def}}{=} \frac{1}{T}\int_0^T \mathrm{E}\{\,\|\boldsymbol{s}(t)\|^2\,\}\mathrm{d}t = \frac{\sigma_a^2}{T}E_{\mathrm{T}} = \frac{E_{\mathrm{s}}}{T}. \tag{10}$$

Since, see above, the variance of the data symbols σ_a^2 is fixed to 1, the transmit power P is directly adjusted via the pulse energy E_{T}. The corresponding quantities related to one of the interferers are indicated by the subscript ν.

2) Optical Channel: The electrical-to-optical (E/O) conversion is performed by an ideal dual-polarization (DP) inphase-quadrature (IQ) converter. The two elements of the transmit signal $\boldsymbol{s}_\nu(t)$ correspond to the modulated *optical* signals in the x- and y-polarization. The *optical field envelope* $\boldsymbol{u}_\nu(z,t)$ of each wavelength channel

$$\boldsymbol{u}_\nu(0,t) = \boldsymbol{s}_\nu(t)\exp(\mathrm{j}\Delta\omega_\nu t), \tag{11}$$

is modulated at its angular carrier frequency $\omega_\nu = \omega_0 + \Delta\omega_\nu$ at the input of the optical transmission line $z = 0$. Here, $\omega_0 = 2\pi f_0$ is the center frequency of the signaling regime of interest. For the probe channel, we require that the carrier frequency ω_ρ coincides with ω_0 such that $\Delta\omega_\rho = 0$ and $\boldsymbol{u}_\rho(0,t) = \boldsymbol{s}_\rho(t)$. The transmitter frontend of the probe channel is shown in Fig. 2 (a).

The N_{ch} wavelength signals $\boldsymbol{u}_\nu(0,t)$ at $z = 0$ are combined by an ideal optical multiplexer to a single WDM signal, cf. Fig. 2 (b). The optical field envelope before transmission is then

$$\boldsymbol{u}(0,t) = \sum_{\nu=1}^{N_{\mathrm{ch}}}\boldsymbol{u}_\nu(0,t) = \sum_{\nu=1}^{N_{\mathrm{ch}}}\boldsymbol{s}_\nu(t)\exp(\mathrm{j}\Delta\omega_\nu t) \tag{12}$$

$$\boldsymbol{U}(0,\omega) = \sum_{\nu=1}^{N_{\mathrm{ch}}}\boldsymbol{U}_\nu(0,\omega) = \sum_{\nu=1}^{N_{\mathrm{ch}}}\boldsymbol{S}_\nu(\omega-\Delta\omega_\nu), \tag{13}$$

with the Fourier pairs $\boldsymbol{s}_\nu(t) \circ\!\!-\!\!\bullet\, \boldsymbol{S}_\nu(\omega)$ and $\boldsymbol{u}(0,t) \circ\!\!-\!\!\bullet\, \boldsymbol{U}(0,\omega)$. Any initial phase and laser phase noise (PN) are neglected to focus only on deterministic distortions.

The optical field envelope is the ECB representation of the *optical field* $\boldsymbol{u}_{\mathrm{o}}(z,t)$ in the passband notation

$$\boldsymbol{u}_{\mathrm{o}}(z,t) \overset{\text{def}}{=} \boldsymbol{u}(z,t)\cdot\exp(\mathrm{j}\omega_0 t - \mathrm{j}\beta_0(z)z), \tag{14}$$

which is known as the *slowly varying amplitude approximation* [15, Eq. (2.4.5)]. For consistency of notation we treat the optical field envelope as a dimensionless entity (in accordance with the electrical signals). The optical field propagates in z-direction (the dimension z has units of *meter*) with the *local* propagation constant $\beta_0(z) = \beta(z,\omega_0)$, and $\beta(z,\omega)$ is the space and frequency-dependent propagation constant. A Taylor expansion of $\beta(z,\omega)$ is performed around ω_0 with

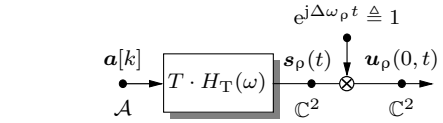

(a) Transmitter frontend of the *probe*

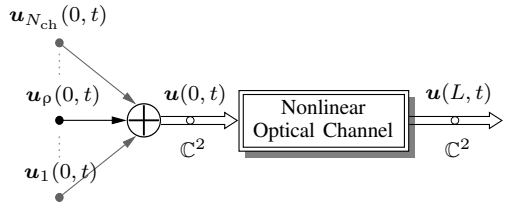

(b) Optical channel

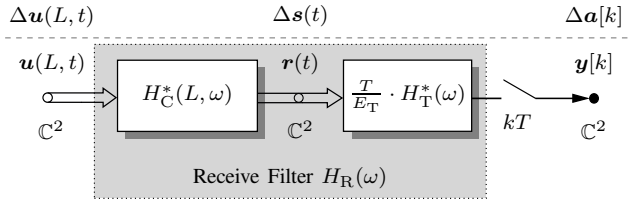

(c) Receiver frontend of the *probe* and variables (top row) associated with the regular perturbation model, cf. Section III

Fig. 2. Components of the generic fiber-optical transmission system model.

the derivatives of $\beta(z,\omega)$ represented by the coefficients [15, Eq. (2.4.4)]

$$\beta_n(z) \overset{\text{def}}{=} \left.\frac{\partial^n\beta(z,\omega)}{\partial\omega^n}\right|_{\omega=\omega_0}, \qquad n\in\mathbb{N}. \tag{15}$$

Here, we only consider coefficients up to second order, i.e., $n \in \{\,0,1,2\,\}$. We also introduce the path-average[4] *dispersion*

[4]We discriminate between *local* (i.e., $\alpha(z)$, $\beta(z)$, $\gamma(z)$) and *path-average* (i.e., α, β, γ) properties of the transmission link. The latter are implicitly indicated if the z-argument of the local property is omitted, e.g., $\beta_2 \triangleq \frac{1}{L}\int_0^L \beta_2(\zeta)\mathrm{d}\zeta$.

length

$$L_{\mathrm{D}} \stackrel{\text{def}}{=} \frac{1}{2\pi|\beta_2|R_{\mathrm{s}}^2}, \tag{16}$$

which denotes the distance after which two spectral components spaced $B = R_{\mathrm{s}}$ *Hertz* apart, experience a differential group delay of $T = 1/R_{\mathrm{s}}$ due to chromatic dispersion (CD). We can equivalently define the walk-off length of the probe and one interfering wavelength channel as

$$L_{\mathrm{wo},\nu} \stackrel{\text{def}}{=} \frac{1}{|\Delta\omega_\nu\beta_2|R_{\mathrm{s}}}, \tag{17}$$

which quantifies the fiber length that must be propagated in order for the νth wavelength channel to walk off by one symbol from the probe channel.

a) Signal Propagation: In the absence of noise, the two dominating effects governing the propagation of the optical signal in the fiber are *dispersion*—expressed by the z-profile of the fiber dispersion coefficient $\beta_2(z)$—and *nonlinear signal-signal interactions*. Generation of the so-termed local NLI depends jointly on the local fiber nonlinearity coefficient $\gamma(z)$ and the z-profile of the optical signal power. For ease of the derivation, we assume that all z-dependent variation in $\gamma(z)$ can be equivalently expressed in a variation of either a local gain $g(z)$ or the local fiber attenuation $\alpha(z)$. We also neglect the time- (and frequency-) dependency of the attenuation, gain, and nonlinearity coefficient.

The interplay between the optical signal, dispersion, and nonlinear interaction is all combined in the noiseless Manakov equation. It is a coupled set of partial differential equations in time-domain for the optical field envelope $\boldsymbol{u}(z,t)$ in the ECB, and the derivative is taken w.r.t. propagation distance $z \in \mathbb{R}$ and to the *retarded time* $t \in \mathbb{R}$. The retarded time is defined as $t \stackrel{\text{def}}{=} t' - z/v_{\mathrm{g}}$, where t' is the *physical* time and v_{g} is the (path-average) group velocity $v_{\mathrm{g}} = 1/\beta_1$ of the probe channel [15, Eq. (2.4.8)]. It can be understood as a time frame that moves at the same average velocity as the probe to cancel out any group delay at the reference frequency $\omega_\rho = \omega_0$. All other frequencies experience a residual group delay relative to the reference frequency due to CD.

The propagation of $\boldsymbol{u}(z,t)$ in the signaling regime of interest is governed by [17, Eq.(6.26)]

$$\frac{\partial}{\partial z}\boldsymbol{u} = \mathrm{j}\frac{\beta_2(z)}{2}\frac{\partial^2}{\partial t^2}\boldsymbol{u} + \frac{g(z)-\alpha(z)}{2}\boldsymbol{u} - \mathrm{j}\gamma(z)\frac{8}{9}\,\|\boldsymbol{u}\|^2\,\boldsymbol{u}. \tag{18}$$

The space- and time-dependency of $\boldsymbol{u}(z,t)$ is omitted here for compact notation. By allowing the local gain coefficient $g(z)$ to contain Dirac δ-functions one can capture the z-dependence of an amplification scheme, i.e., based on lumped erbium-doped fiber amplifier (EDFA) or Raman amplification. Polarization-dependent effects such as birefringence and polarization mode dispersion (PMD) are neglected limiting the following derivations to the practically relevant case of low-PMD fibers. We also assume that all wavelength channels are co-polarized, i.e., modulated on polarization axes parallel to the ones of the probe channel.

b) Dispersion Profile: The accumulated dispersion is a function that satisfies [21, Eq. (8)]

$$\frac{\mathrm{d}\mathcal{B}(z)}{\mathrm{d}z} = \beta_2(z). \tag{19}$$

Here, $\mathcal{B}(z)$ can be used to express a z-dependency in the dispersion profile, i.e., lumped dispersion compensation by in-line dispersion compensation or simply a transmission link with distinct fiber properties across multiple spans. We obtain

$$\mathcal{B}(z) = \int_0^z \beta_2(\zeta)\mathrm{d}\zeta + \mathcal{B}_0, \tag{20}$$

where $\mathcal{B}_0 \stackrel{\text{def}}{=} \mathcal{B}(0)$ is the amount of pre-dispersion (in units of squared *seconds*, typically given in ps^2) at the beginning of the transmission line.

c) Power Profile: To describe the power evolution of $\boldsymbol{u}(z,t)$, we introduce the *normalized* power profile $\mathcal{P}(z)$ as a function that satisfies the equation [21, Eq. (7)]

$$\frac{\mathrm{d}\mathcal{P}(z)}{\mathrm{d}z} = (g(z)-\alpha(z))\;\mathcal{P}(z), \tag{21}$$

with boundary condition $\mathcal{P}(0) = \mathcal{P}(L) = 1$, i.e., the last optical amplifier resets the signal power to the transmit power. The z-dependence on $\alpha(z)$ allows for varying attenuation coefficients over different spans. In writing (21) we assumed that both the local gain coefficient and attenuation coefficient are frequency-independent. We may also define the logarithmic gain/loss profile as

$$\mathcal{G}(z) \stackrel{\text{def}}{=} \ln\left(\mathcal{P}(z)\right) = \int_0^z (g(\zeta)-\alpha(\zeta))\;\mathrm{d}\zeta. \tag{22}$$

The last expression in (22) is obtained by solving (21) for $\mathcal{P}(z) = \mathrm{e}^{\mathcal{G}(z)}$. The boundray conditions on $\mathcal{P}(z)$ immediately give the boundary condition $\mathcal{G}(0) = \mathcal{G}(L) = 0$.

We can now define the impulse response and transfer function of the *linear* channel—that is, when the fiber nonlinearity coefficient is zero, i.e., $\gamma = 0$ in (18). To that end, we define the optical field envelope $\boldsymbol{u}_{\mathrm{LIN}}(z,t) \circ\!\!-\!\!\bullet\, \boldsymbol{U}_{\mathrm{LIN}}(z,\omega)$ that propagates solely according to linear effects with the boundary condition $\boldsymbol{u}_{\mathrm{LIN}}(0,t) = \boldsymbol{u}(0,t)$ at the input of the transmission link. The *linear* channel transfer function and impulse response is then given by

$$H_{\mathrm{C}}(z,\omega) \stackrel{\text{def}}{=} \exp\left(\frac{\mathcal{G}(z) - \mathrm{j}\omega^2\mathcal{B}(z)}{2}\right) \tag{23}$$

$$\vdots$$

$$h_{\mathrm{C}}(z,t) = \frac{1}{\sqrt{2\pi}}\frac{1}{\sqrt{\mathrm{j}\mathcal{B}(z)}}\exp\left(\frac{\mathcal{G}(z) + \mathrm{j}t^2/\mathcal{B}(z)}{2}\right), \tag{24}$$

which represents the joint effect of chromatic dispersion and the gain/loss variation along the link. We finally have the linear channel relation in time-domain $\boldsymbol{u}_{\mathrm{LIN}}(z,t) = h_{\mathrm{C}}(z,t) * \boldsymbol{u}_{\mathrm{LIN}}(0,t)$ and frequency-domain $\boldsymbol{U}_{\mathrm{LIN}}(z,\omega) = H_{\mathrm{C}}(z,\omega)\boldsymbol{U}_{\mathrm{LIN}}(0,\omega)$, which will be used in the next section in the context of the first-order perturbation method.

3) Receiver Frontend: Again, we assume ideal optical-to-electrical (O/E) and analog-to-digital (A/D) conversion. The received continuous-time, optical signal $\boldsymbol{u}(L,t)$ is first matched filtered w.r.t. the *linear* channel response and transmit pulse, and then sampled at the symbol period T to obtain the discrete-time receive symbols $\boldsymbol{y}[k]$, cf. Fig. 2 (c). The receiver frontend hence also compensates for any residual link loss and performs perfect CD compensation. Note, that the analog frontend is usually realized using an oversampled digital representation. E.g., CD compensation is typically performed in the (oversampled) digital domain. Here, we prefer to conceptually incorporate it in the analog domain since it significantly simplifies notation in the derivation of the end-to-end channel model. The transfer function of the entire cascade of the receiver frontend is given by

$$H_{\mathrm{R}}(\omega) = \frac{T}{E_{\mathrm{T}}} H_{\mathrm{C}}^{*}(L,\omega) H_{\mathrm{T}}^{*}(\omega). \tag{25}$$

Due to $\mathcal{P}(L) = 1$ and the pre-factor T/E_{T}, the received signal is re-normalized to the variance of the constellation σ_a^2. Since we only consider T-spaced sampling any fractional sampling phase-offset or timing synchronization[5] is already incorporated as suited delay in the receive filter $h_{\mathrm{R}}(t)$, s.t. the transmitted and received sequence of the probe are perfectly aligned in time.

III. First-Order Perturbation

The principle philosophy of fiber-optical channel models based on the perturbation method is to assume that nonlinear distortions are *weak* compared to its source, i.e., the propagating signal. Starting from this premise the regular perturbation (RP) ansatz for the optical end-to-end channel is written as

$$\boldsymbol{u}(L,t) = \boldsymbol{u}_{\mathrm{LIN}}(L,t) + \Delta\boldsymbol{u}(L,t), \tag{26}$$

where $\boldsymbol{u}_{\mathrm{LIN}}(z,t) \in \mathbb{C}^2$ is the signal propagating according to the linear effects, i.e., according to (23), (24). In this context, the nonlinear distortion $\Delta\boldsymbol{u}(z,t) \in \mathbb{C}^2$ is termed *perturbation*, which is generated locally according to nonlinear signal-signal interaction and is then propagated linearly and independently of the signal $\boldsymbol{u}_{\mathrm{LIN}}(z,t)$ to the end of the optical channel at $z = L$. We assume that the optical perturbation at $z = 0$ is zero, i.e., $\Delta\boldsymbol{u}(0,t) = 0$. The received signal is then given as the sum of the solution for the linearly propagating signal and the accumulated perturbation representing the accumulated nonlinear effects.

The objective of this section is to develop the input/output relation of the equivalent discrete-time end-to-end channel in the form of

$$\boldsymbol{y}[k] = \boldsymbol{a}[k] + \Delta\boldsymbol{a}[k], \tag{27}$$

where the total NLI is absorbed into a single *discrete-time* perturbative term $\Delta\boldsymbol{a}[k]$, cf. Fig. 2 (c). To that end, we start with a known RP solution of the optical end-to-end relation and successively incorporate the required components according to Fig. 1 and Fig. 2.

[5]Note, that the time delay L/v_{g} at ω_0 and any initial phase β_0 has already been canceled from the propagation equation in (18).

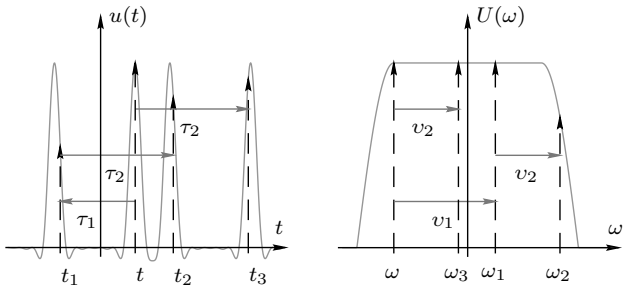

(a) Time-domain (b) Frequency-domain

Fig. 3. Definitions of variables in the time- and frequency-domain. Note, that both τ_1, τ_2 and υ_1, υ_2 can take positive and negative values in $\mathbb{R}$.

A. Optical End-to-End Channel

The solution to the optical perturbation after transmission at $z = L$ is given in frequency-domain by [4, Eq. (12)], [22, Eq. (2)], [23, Eq. (4)], [24, Eq. (24)–(27)]

$$\Delta\boldsymbol{U}(L,\omega) = -\mathrm{j}\gamma\frac{8}{9}\frac{L_{\mathrm{eff}}}{(2\pi)^2} H_{\mathrm{C}}(L,\omega) \times \int_{\mathbb{R}^2} \underline{\boldsymbol{U}}(\omega,\upsilon_1,\upsilon_2) H_{\mathrm{NL}}(\upsilon_1,\upsilon_2)\,\mathrm{d}^2\boldsymbol{\upsilon}, \tag{28}$$

with the normalized *nonlinear transfer function* $H_{\mathrm{NL}}(\upsilon_1,\upsilon_2)$ and $\underline{\boldsymbol{U}}(\omega,\upsilon_1,\upsilon_2) \overset{\text{def}}{=} \boldsymbol{U}(0,\omega+\upsilon_2)\boldsymbol{U}^{\mathsf{H}}(0,\omega+\upsilon_1+\upsilon_2)\boldsymbol{U}(0,\omega+\upsilon_1)$, i.e., a term that depends on the optical field envelope at the *input* of the transmission system. Note, that we made use of the common variable substitution

$$\omega_1 \overset{\text{def}}{=} \omega + \upsilon_1 \tag{29}$$

$$\omega_2 \overset{\text{def}}{=} \omega + \upsilon_1 + \upsilon_2 \tag{30}$$

$$\omega_3 \overset{\text{def}}{=} \omega - \omega_1 + \omega_2 = \omega + \upsilon_2, \tag{31}$$

to express the field $\boldsymbol{U}$ in terms of difference frequencies υ_1 and υ_2 relative to ω. Fig. 3 summarizes the definitions of the time- and frequency variables that are used throughout this text[6].

Equation (28) shows that the first-order RP method can be understood as a FWM process with un-depleted *pumps* where three wavelengths affect a fourth. Equivalently, one can think of the joint annihilation and creation of two two-photon pairs (i.e., with four frequencies involved) preserving both energy (*frequency matching*)[7] and momentum (*phase matching*) during the interaction [25, Fig. 7.2.5].

The normalized nonlinear transfer function is a measure of the phase matching condition and defined as

$$H_{\mathrm{NL}}(\upsilon_1,\upsilon_2) \overset{\text{def}}{=} \frac{1}{L_{\mathrm{eff}}}\int_0^L \exp\left(\mathcal{G}(\zeta) + \mathrm{j}\upsilon_1\upsilon_2\mathcal{B}(\zeta)\right)\mathrm{d}\zeta = \frac{1}{L_{\mathrm{eff}}}\int_0^L H_{\mathrm{C}}^{*}(\zeta,\sqrt{\upsilon_1\upsilon_2})^2\,\mathrm{d}\zeta. \tag{34}$$

The pre-factor is the *effective length* of the *whole* transmission link defined as

$$L_{\mathrm{eff}} \overset{\text{def}}{=} \int_0^L \mathcal{P}(\zeta)\,\mathrm{d}\zeta = \int_0^L \exp(\mathcal{G}(\zeta))\,\mathrm{d}\zeta, \tag{35}$$

[6]The integral over $\mathbb{R}^2$ in (28) can also be performed w.r.t. ω_1 and ω_2.

[7]The conjugate field corresponds to the inverse process where photon creation and annihilation is interchanged.

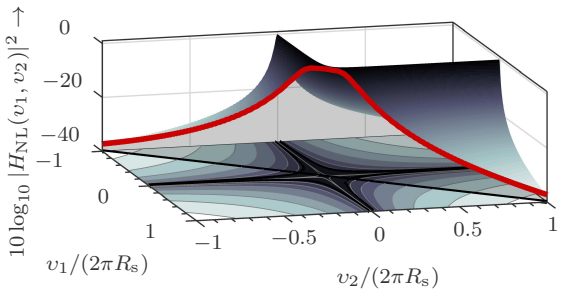

Fig. 4. Magnitude in logarithmic scale of the *single-span* nonlinear transfer function for $\beta_2 = -21$ ps^2/km, $\mathcal{B}_0 = 0$ ps^2, $10\log_{10}\mathrm{e}^{\alpha} = 0.2$ dB/km and $L_{\mathrm{sp}} = 100$ km over the *difference* frequencies υ_1 and υ_2 normalized to $R_{\mathrm{s}} = 64$ GBd. The red line denotes $H_{\mathrm{NL}}(\xi)$ which only depends on the scalar $\xi = \upsilon_1\upsilon_2$. (Part for $\upsilon_1 > \upsilon_2$ not shown).

and acts as a normalization constant s.t. $H_{\mathrm{NL}}(0,0) = 1$.

The *phase mismatch* $\Delta\beta$, i.e., the difference in the (path-average) propagation constant due to dispersion, is defined as [15, Eq. (6.3.19)]

$$\begin{aligned}\Delta\beta &\stackrel{\text{def}}{=} \beta(\omega) - \beta(\omega_1) + \beta(\omega_2) - \beta(\omega_3)\\ &= \frac{\beta_2}{2}(\omega^2 - \omega_1^2 + \omega_2^2 - (\omega - \omega_1 + \omega_2)^2)\\ &= \beta_2(\omega_1 - \omega)(\omega_2 - \omega_1) = \beta_2\upsilon_1\upsilon_2, \end{aligned} \tag{36}$$

where the propagation constants at the four frequencies are developed in a second-order Taylor series according to (15). E.g., for transmission systems without inline dispersion compensation and zero pre-dispersion $\mathcal{B}_0 = 0$, we have $\mathcal{B}(z) = \beta_2 z$ and the phase mismatch $\Delta\beta$ can be found in the argument of the exponential in (34) with $\upsilon_1\upsilon_2\,\mathcal{B}(z) = \Delta\beta\, z$.

In the context of the equivalent ansatz following the regular VSTF [3], [4], [24], the nonlinear transfer function $H_{\mathrm{NL}}(\upsilon_1,\upsilon_2)$ is also referred to as 3rd-order Volterra *kernel*. Closed form analytical solutions to (34) can be obtained for single-span or homogeneous multi-span systems [24], [26]. It is noteworthy, that $H_{\mathrm{NL}}(\upsilon_1,\upsilon_2)$ contains all information about the transmission link characterized by the dispersion profile (including CD pre-compensation $\mathcal{B}_0$, cf. (20)) and the gain/loss profile.

Fig. 4 shows the magnitude of $H_{\mathrm{NL}}(\upsilon_1,\upsilon_2)$ (in logarithmic scale) exemplifying a single-span standard single-mode fiber (SSMF) link. Note, that $H_{\mathrm{NL}}(\upsilon_1,\upsilon_2)$ depends in fact on the product $\xi \stackrel{\text{def}}{=} \upsilon_1\upsilon_2$ and is hence a hyperbolic function in two dimensions [27, Sec. VIII] (cf. the contour in Fig. 4). The bold red line drawn into the diagonal cross section in Fig. 4 is the corresponding nonlinear transfer function $H_{\mathrm{NL}}(\xi)$ which only depends on the scalar variable $\xi = \upsilon_1\upsilon_2$.

Fig. 5 shows the magnitude of $H_{\mathrm{NL}}(\xi)$ (in logarithmic scale) over the normalized variable $\xi/(2\pi R_{\mathrm{s}})^2$ to relate the nonlinear transfer function to the spectral width of the probe channel. The spectral width of $|H_{\mathrm{NL}}(\xi/(2\pi R_{\mathrm{s}})^2)|^2$ is proportional to the inverse dimensionless *map strength* $1/\mathcal{S}_{T,\rho} \stackrel{\text{def}}{=} L_{\mathrm{D}}/L_{\mathrm{eff}}$ closely related to the *nonlinear diffusion bandwidth* defined in [22]. Conversely, the map strength $\mathcal{S}_{T,\rho}$ quantifies the number of nonlinearly interacting pulses in time over the effective length L_{eff} within the probe channel [28]. It is therefore a direct measure of *intra-channel* (i.e., SCI) nonlinear effects [29]. The relevant quantity for *inter-channel* (i.e., XCI) effects is given by $\mathcal{S}_{T,\nu} \stackrel{\text{def}}{=} L_{\mathrm{eff}}/L_{\mathrm{wo},\nu}$ (with $\nu \neq \rho$) where the temporal walk-off between wavelength channels is the relevant length scale. In [23] it was shown that $H_{\mathrm{NL}}(\xi)$ is related to the power-weighted dispersion distribution (PWDD) by a (one-dimensional) Fourier transformation (w.r.t. the scalar variable ξ) and has a time-domain counterpart which is discussed in the next paragraph.

B. Electrical End-to-End Channel

To derive the discrete-time end-to-end channel model the filter cascade of the linear receiver frontend is subsequently applied to $\Delta\boldsymbol{U}(L,\omega)$. The perturbation $\Delta\boldsymbol{S}(\omega)$ (i.e., the perturbation in the *electrical* domain following our terminology, cf. Fig. 2 (c)) is obtained by

$$\Delta\boldsymbol{S}(\omega) = H_{\mathrm{C}}^*(L,\omega)\Delta\boldsymbol{U}(L,\omega), \tag{39}$$

which cancels out the leading term $H_{\mathrm{C}}(L,\omega)$ in (28) since $|H_{\mathrm{C}}(L,\omega)| = 1$. The result is shown in (32) at the bottom of the next page. Remarkably, there exists an equivalent time-domain representation $\Delta\boldsymbol{s}(t) \circ\!\!-\!\!\bullet\, \Delta\boldsymbol{S}(\omega)$ shown in (33) where the Fourier relation is derived in Appendix A. The time-domain perturbation $\Delta\boldsymbol{s}(t)$ has the same form as its frequency-domain counterpart, i.e., the integrand is constituted by the respective time-domain representation of the optical signal and the double integral is performed over the time variables τ_1 and τ_2 (cf. Fig. 3 (a) and [23], [30]).

The frequency matching with $\omega_3 \stackrel{\text{def}}{=} \omega - \omega_1 + \omega_2$ is translated to a *temporal matching*[8] $t_3 \stackrel{\text{def}}{=} t - t_1 + t_2$ (cf. [31]), i.e., the selection rules of FWM apply both in time and frequency. Remarkably, the time-domain *kernel* $h_{\mathrm{NL}}(\tau_1,\tau_2)$ is related to $H_{\mathrm{NL}}(\upsilon_1,\upsilon_2)$ by an inverse two-dimensional (2D) Fourier transform (cf. [30, Appx.] and [28, Eq. (6)]) which can be written as

$$\begin{aligned} h_{\mathrm{NL}}(\tau_1,\tau_2) &= h_{\mathrm{NL}}(\boldsymbol{\tau}) = \mathcal{F}^{-1}\{H_{\mathrm{NL}}(\boldsymbol{\upsilon})\}\\ &= \frac{1}{L_{\mathrm{eff}}}\int_0^L \frac{1}{2\pi|\mathcal{B}(\zeta)|}\exp\left(\mathcal{G}(\zeta) - \mathrm{j}\frac{\tau_1\tau_2}{\mathcal{B}(\zeta)}\right)\mathrm{d}\zeta\\ &\stackrel{\mathcal{B}(z)\leq 0}{=} \frac{\mathrm{j}}{L_{\mathrm{eff}}}\int_0^L h_{\mathrm{C}}^*(\zeta,\sqrt{\tau_1\tau_2})^2\,\mathrm{d}\zeta, \end{aligned} \tag{40}$$

with the tuples $\boldsymbol{\tau} = [\tau_1,\tau_2]^{\mathsf{T}}$ and $\boldsymbol{\upsilon} = [\upsilon_1,\upsilon_2]^{\mathsf{T}}$. The time-domain kernel maintains its hyperbolic form as it is a function of the product $\tau_1\tau_2$. Also note the duality to (34), where in both representations the nonlinear transfer function can be understood as the *path-average* (cf. [32]) over an expression related to the linear channel response $h_{\mathrm{C}}(z,t) \circ\!\!-\!\!\bullet\, H_{\mathrm{C}}(z,\omega)$. Note, that in (40) the condition on $\mathcal{B}(z) \leq 0$ (which is typically fulfilled in the anomalous dispersion regime with $\beta_2 < 0$) is required to obtain the simple result without cumbersome differentiation of the term $|\mathcal{B}(z)|$.

The next step is to dissect the perturbation $\Delta\boldsymbol{s}(t) \circ\!\!-\!\!\bullet\, \Delta\boldsymbol{S}(\omega)$ into contributions originating from SCI, XCI, or multi-channel interference (MCI). We notice from Fig. 5 that, given R_{s} is sufficiently large, $|H_{\mathrm{NL}}(\xi)|^2$ vanishes if $\xi \gg (2\pi R_{\mathrm{s}})^2$, i.e., if the *phase matching condition*

[8] Not to be confused with the phase matching condition in (34), (36).

is not properly met. Conversely, if the spectral width of $|H_{\mathrm{NL}}(\xi/R_{\mathrm{s}}^2)|^2$ (or equivalently the inverse map strength $1/\mathcal{S}_{T,\rho}$) is small enough, the integrand in (32), (33) can be factored into a SCI and XCI term, i.e., mixing terms that originate either from within the probe channel (both $\upsilon_1 < 2\pi R_{\mathrm{s}}$ and $\upsilon_2 < 2\pi R_{\mathrm{s}}$) or from within the probe channel and a single interfering wavelength channel (either $\upsilon_1 < 2\pi R_{\mathrm{s}}$ or $\upsilon_2 < 2\pi R_{\mathrm{s}}$). Mixing terms originating from MCI are only relevant for small R_{s}. We hence neglect any FWM terms involving more than two wavelength channels.

The optical field envelope $\boldsymbol{u}(0,t) \circ\!\!-\!\!\bullet\, \boldsymbol{U}(0,\omega)$ in (32), (33) is now expanded according to (12), (13). By definition we have $\Delta\omega_\rho = 0$ and we can expand the triple product of $\boldsymbol{U}(0,\omega)$ in (32) as

$$\boldsymbol{U}\boldsymbol{U}^{\mathsf{H}}\boldsymbol{U} = \underbrace{\boldsymbol{U}_\rho \boldsymbol{U}_\rho^{\mathsf{H}} \boldsymbol{U}_\rho}_{\mathrm{SCI}} + \sum_{\nu\neq\rho} \underbrace{\Big(\boldsymbol{U}_\nu \boldsymbol{U}_\nu^{\mathsf{H}} \boldsymbol{U}_\rho + \boldsymbol{U}_\rho \boldsymbol{U}_\nu^{\mathsf{H}} \boldsymbol{U}_\nu\Big)}_{\mathrm{XCI}} \tag{41}$$

where the frequency-dependency of $\boldsymbol{U}(0,\omega)$ is omitted for short notation. The XCI term has two contributions—the first results from an interaction where ω_3 and ω_2 are from the νth interfering wavelength channel and ω and ω_1 are within the probe's support ($\upsilon_2 \to \Delta\omega_\nu$ in Fig. 3 (b)). The second involves an interaction where ω_2 and ω_1 are from the interfering wavelength channel and ω and ω_3 are from the probe channel ($\upsilon_1 \to \Delta\omega_\nu$).

We can exploit the symmetry of the nonlinear transfer function $H_{\mathrm{NL}}(\upsilon_1,\upsilon_2) = H_{\mathrm{NL}}(\upsilon_2,\upsilon_1)$ to simplify the XCI expression in (41). We obtain with the definition of the electrical signal of each wavelength channel (cf. (12), (13)) after rearranging some terms[9]

$$\begin{aligned}
&\boldsymbol{U}(0,\,\omega_3)\boldsymbol{U}^{\mathsf{H}}(0,\omega_2)\boldsymbol{U}(0,\omega_1)H_{\mathrm{NL}}(\omega_2-\omega_3,\omega_2-\omega_1)\\
&\quad= \boldsymbol{S}_\rho(\omega_1)\boldsymbol{S}_\rho^{\mathsf{H}}(\omega_2)\boldsymbol{S}_\rho(\omega_3)H_{\mathrm{NL}}(\omega_2-\omega_1,\omega_2-\omega_3)\\
&\qquad+\sum_{\nu\neq\rho}\Big(\boldsymbol{S}_\nu(\omega_1)\boldsymbol{S}_\nu^{\mathsf{H}}(\omega_2)+\boldsymbol{S}_\nu^{\mathsf{H}}(\omega_2)\boldsymbol{S}_\nu(\omega_1)\mathbf{I}\Big)\boldsymbol{S}_\rho(\omega_3)\\
&\qquad\times H_{\mathrm{NL}}(\underbrace{\omega_2-\omega_1}_{\upsilon_2},\underbrace{\omega_2-\omega_3}_{\upsilon_1}-\Delta\omega_\nu),
\end{aligned}\tag{42}$$

which now corresponds to the case that ω_3 always lays in the support of the probe[10]. The signals of the interfering wavelength channels are now represented in their respective ECB and the relative frequency offset $\Delta\omega_\nu$ is accounted for via the modified argument of $H_{\mathrm{NL}}(\cdot,\cdot)$.

At this point, considering (32) and (42), we formulated the relation between the perturbation at the probe $\Delta\boldsymbol{S}(\omega)$ after chromatic dispersion compensation and the transmit spectra $\boldsymbol{S}_\nu(\omega)$ of the probe and the interferers in their respective baseband. The remaining operation in the receiver cascade is to perform matched filtering w.r.t. the transmit pulse and then to perform T-spaced sampling.

C. Discrete-Time End-to-End Channel

We recap that the periodic spectrum $X(\mathrm{e}^{\mathrm{j}\omega T})$ of the sampled signal $x[k] \overset{\text{def}}{=} x(kT)$ is related to the *aliased* spectrum of the continuous-time signal $x(t)$ over the Nyquist interval $\mathbb{T}$ by

$$X(\mathrm{e}^{\mathrm{j}\omega T}) \overset{\text{def}}{=} \textsc{Alias}\{\, X(\omega)\,\} = \frac{1}{T}\sum_{m\in\mathbb{Z}} X(\omega - \frac{2\pi m}{T}). \tag{43}$$

The matched filter $H_{\mathrm{T}}^*(\omega)$ and the *aliasing operator* are used to translate (32), (33) to the equivalent discrete-time form in (37), (38) exemplarily for the SCI contribution $\Delta\boldsymbol{a}^{\mathrm{SCI}}$. The total perturbation inflicted on the probe channel is $\Delta\boldsymbol{a}[k] = \Delta\boldsymbol{a}^{\mathrm{SCI}}[k] + \Delta\boldsymbol{a}^{\mathrm{XCI}}[k]$.

In (37), (38) we use the $1/T$-periodic spectrum $\boldsymbol{A}(\mathrm{e}^{\mathrm{j}\omega T})$ which is related to the discrete-time sequence $\langle\, \boldsymbol{a}[k]\,\rangle$ by a DTFT $\boldsymbol{A}(\mathrm{e}^{\mathrm{j}\omega T}) = \hat{\mathcal{F}}\{\, \boldsymbol{a}[k]\,\}$. The channel-dependent *nonlinear length* is $L_{\mathrm{NL},\nu} \overset{\text{def}}{=} 1/(\gamma P_\nu)$ and $P_\nu = \frac{\sigma_{b,\nu}^2}{T} E_{\mathrm{T},\nu}$ is the optical launch power of the νth wavelength channel. The normalized *nonlinear* end-to-end transfer function $H_\nu(\boldsymbol{\omega}) = H_\nu(\omega_1,\omega_2,\omega_3)$ characterizes the nonlinear cross-talk from the νth wavelength channel to the probe channel. In particular, $H_\rho(\boldsymbol{\omega})$ describes SCI and $H_\nu(\boldsymbol{\omega})$ with $\nu\neq\rho$ describes XCI. It is defined as

$$\begin{aligned}
H_\nu(\boldsymbol{\omega}) \overset{\text{def}}{=}\; & T\cdot H_{\mathrm{T},\nu}(\omega_1)\; T\cdot H_{\mathrm{T},\nu}^*(\omega_2)\;/\;P_\nu\\
&\times T\cdot H_{\mathrm{T},\rho}(\omega_3)\; T\cdot H_{\mathrm{T},\rho}^*(\omega_1-\omega_2+\omega_3)\;/\;E_{\mathrm{T},\rho}\\
&\times H_{\mathrm{NL}}(\omega_2-\omega_1,\omega_2-\omega_3-\Delta\omega_\nu),
\end{aligned}\tag{44}$$

and its *periodic continuation*, i.e., the aliased discrete-time equivalent is given by

$$H_\nu(\mathrm{e}^{\mathrm{j}\boldsymbol{\omega}T}) = \frac{1}{T^3}\sum_{\boldsymbol{m}\in\mathbb{Z}^3} H_\nu(\boldsymbol{\omega} - \frac{2\pi\boldsymbol{m}}{T}), \tag{45}$$

where the three-fold aliasing is done along each frequency dimension with $\boldsymbol{\omega} = [\omega_1,\omega_2,\omega_3]^{\mathsf{T}}$ and $\boldsymbol{m} = [m_1,m_2,m_3]^{\mathsf{T}}$. The normalization[11] in (44) is done s.t. $H_\rho(\mathrm{e}^{\mathrm{j}\mathbf{0}T}) = 1$ and

[9] Since $\boldsymbol{U}_\nu^{\mathsf{H}}\boldsymbol{U}_\nu$ is a scalar, we have $\boldsymbol{U}_\rho\boldsymbol{U}_\nu^{\mathsf{H}}\boldsymbol{U}_\nu = \boldsymbol{U}_\nu^{\mathsf{H}}\boldsymbol{U}_\nu\boldsymbol{U}_\rho$. The 2×2 identity matrix $\mathbf{I}$ is required to factor the XCI expression in a ν- and ρ-dependent term.

[10] An alternative formulation with ω_1 in the support of the probe is obtained by exchanging the subscripts of ω_1 and ω_3 in frequency-domain and t_1 and t_3 in time-domain.

[11] Note, that by definition the optical launch power P_ν of the νth wavelength channel is related to the pulse energy of $H_{\mathrm{T},\nu}(\omega)$ in (9), (10).

$$\Delta\boldsymbol{S}(\omega) = -\mathrm{j}\gamma\frac{8}{9}L_{\mathrm{eff}}\frac{1}{(2\pi)^2}\int_{\mathbb{R}^2}\boldsymbol{U}(0,\underbrace{\omega+\upsilon_2}_{\omega_3=\omega-\omega_1+\omega_2})\boldsymbol{U}^{\mathsf{H}}(0,\underbrace{\omega+\upsilon_1+\upsilon_2}_{\omega_2})\boldsymbol{U}(0,\underbrace{\omega+\upsilon_1}_{\omega_1})H_{\mathrm{NL}}(\upsilon_1,\upsilon_2)\,\mathrm{d}^2\boldsymbol{\upsilon} \tag{32}$$

$$\Delta\boldsymbol{s}(t) = -\mathrm{j}\gamma\frac{8}{9}L_{\mathrm{eff}}\int_{\mathbb{R}^2}\boldsymbol{u}(0,\underbrace{t+\tau_1}_{t_1})\boldsymbol{u}^{\mathsf{H}}(0,\underbrace{t+\tau_1+\tau_2}_{t_2})\boldsymbol{u}(0,\underbrace{t+\tau_2}_{t_3=t-t_1+t_2})h_{\mathrm{NL}}(\tau_1,\tau_2)\,\mathrm{d}^2\boldsymbol{\tau} \tag{33}$$

$\mathcal{F}_{\boldsymbol{\tau}\leftrightarrow\boldsymbol{\upsilon}}\{\,\cdot\,\}$

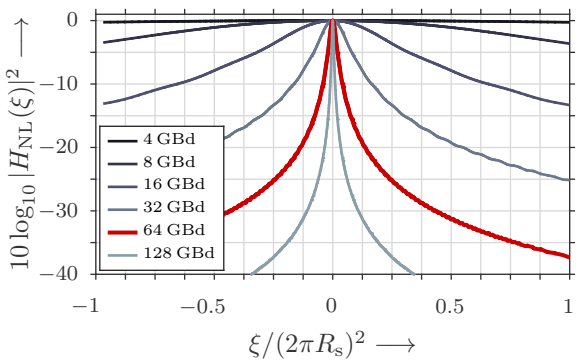

Fig. 5. Magnitude in logarithmic scale of the *single-span* nonlinear transfer function for $\beta_2 = -21$ ps^2/km, $\mathcal{B}_0 = 0$ ps^2, $10\log_{10}\mathrm{e}^{\alpha} = 0.2$ dB/km and $L_{\mathrm{sp}} = 100$ km over $\xi = \upsilon_1\upsilon_2$. The normalization by $(2\pi R_{\mathrm{s}})^2$ relates $H_{\mathrm{NL}}(\xi)$ to the probe's spectral width. The width of $|H_{\mathrm{NL}}(\xi/R_{\mathrm{s}}^2)|^2$ is then proportional to $1/\mathcal{S}_{T,\rho} = L_{\mathrm{D}}/L_{\mathrm{eff}} \propto R_{\mathrm{s}}^{-2}$, i.e., doubling R_{s} reduces the spectral width by a factor of 4.

dimensionless. The nonlinear end-to-end transfer function in (44) depends on the characteristics of the transmission link, comprised by $H_{\mathrm{NL}}(\cdot,\cdot)$, the characteristics of the pulse-shapes of the probe and interfering wavelength channel (assuming matched filtering w.r.t. the channel and the probe's transmit pulse) and the frequency offset $\Delta\omega_\nu$ between probe and interferer.

It is remarkable that the integration in (37) is over the two-fold tuple $[\omega_1,\omega_2]^{\mathsf{T}} \in \mathbb{T}^2$ while the time-domain summation in (38) is over three independent variables $\boldsymbol{\kappa} = [\kappa_1,\kappa_2,\kappa_3]^{\mathsf{T}} \in \mathbb{Z}^3$. This is a consequence of the time-frequency relation between convolution and element-wise multiplication. The temporal matching required for the *optical field* in (33) is now canceled in (38) due to the convolution with the matched filter $h_{\mathrm{T}}^*(-t)$, i.e., κ_3 does not depend on κ_1 and κ_2 unlike $t_3 \overset{\text{def}}{=} t - t_1 + t_2$. Note, that the frequency variable ω_3 in (37) still complies with the frequency matching $\omega_3 = \omega - \omega_1 + \omega_2$ but may be outside the Nyquist interval $\mathbb{T}$. Due to the $1/T$-periodicity of the spectrum $\boldsymbol{A}(\mathrm{e}^{\mathrm{j}\omega T})$ any frequency component outside $\mathbb{T}$ is effectively *folded* back into the Nyquist interval by addition of integer multiples of ω_{Nyq} (denoted by the $\textsc{Fold}\{\cdot\}$ operation in (37)).

The XCI complement to (37) reads

$$\begin{aligned}\Delta\boldsymbol{A}^{\mathrm{XCI}}(\mathrm{e}^{\mathrm{j}\omega T}) = -\mathrm{j}\sum_{\nu\neq\rho}\frac{8}{9}\frac{L_{\mathrm{eff}}}{L_{\mathrm{NL},\nu}}\frac{T^2}{(2\pi)^2}\int_{\mathbb{T}^2}\\ \times\Big(\boldsymbol{B}_\nu(\mathrm{e}^{\mathrm{j}\omega_1 T})\boldsymbol{B}_\nu^{\mathsf{H}}(\mathrm{e}^{\mathrm{j}\omega_2 T}) + \boldsymbol{B}_\nu^{\mathsf{H}}(\mathrm{e}^{\mathrm{j}\omega_2 T})\boldsymbol{B}_\nu(\mathrm{e}^{\mathrm{j}\omega_1 T})\mathbf{I}\Big)\\ \times\boldsymbol{A}(\mathrm{e}^{\mathrm{j}\omega_3 T})H_\nu(\mathrm{e}^{\mathrm{j}\boldsymbol{\omega}T})\,\mathrm{d}^2\boldsymbol{\omega}.\end{aligned} \tag{46}$$

The time-domain description of the T-spaced channel model in (38) is equivalent to the *pulse-collision picture* (cf. [13, Eq. (3-4)] and [33, Eq. (3-4)]) and the XCI result is repeated here for completeness

$$\begin{aligned}\Delta\boldsymbol{a}^{\mathrm{XCI}}[k] = -\mathrm{j}\sum_{\nu\neq\rho}\frac{8}{9}\frac{L_{\mathrm{eff}}}{L_{\mathrm{NL},\nu}}\sum_{\boldsymbol{\kappa}\in\mathbb{Z}^3}\Big(\boldsymbol{b}_\nu[k+\kappa_1]\boldsymbol{b}_\nu^{\mathsf{H}}[k+\kappa_2]\\ + \boldsymbol{b}_\nu^{\mathsf{H}}[k+\kappa_2]\boldsymbol{b}_\nu[k+\kappa_1]\mathbf{I}\Big)\boldsymbol{a}[k+\kappa_3]h_\nu[\boldsymbol{\kappa}].\end{aligned} \tag{47}$$

The time-domain and *aliased* frequency-domain kernel are related by a three-dimensional (3D) DTFT according to

$$h_\nu[\boldsymbol{\kappa}] = \hat{\mathcal{F}}^{-1}\{\,H_\nu(\mathrm{e}^{\mathrm{j}\boldsymbol{\omega}T})\,\}. \tag{48}$$

The kernel $h_\nu[\boldsymbol{\kappa}] = h_\nu[\kappa_1,\kappa_2,\kappa_3]$ is equivalent to the kernel derived in the seminal paper by Mecozzi and Essiambre in [10, Eq. (61), (62)] via an alternative approach that instead involves an integration over time and space.

D. Relation to the GN-Model and System Design Rules

Parseval's theorem applied to (48) yields

$$E_{h,\nu} \overset{\text{def}}{=} \sum_{\boldsymbol{\kappa}\in\mathbb{Z}^3}|h_\nu[\boldsymbol{\kappa}]|^2 = \left(\frac{T}{2\pi}\right)^3\int_{\mathbb{T}^3}|H_\nu(\mathrm{e}^{\mathrm{j}\boldsymbol{\omega}T})|^2\,\mathrm{d}^3\boldsymbol{\omega}, \tag{49}$$

where the right-hand side can be interpreted as an alternative formulation of the (frequency-domain) Gaussian noise (GN)-model [27] in $1/T$-periodic continuous-frequency domain[12]. This is the dual representation to the original work where the optical signal is constructed as a continuous-time signal with period T_0 and *discrete* frequency components (c.f. the Karhunen-Loève formula in [26], [34]). In other words, the discretization in one domain and the periodicity in the other is exchanged in (49) compared to the GN-model. In this view, the result obtained by the GN-model corresponds to the *kernel energy* $E_{h,\nu}$ of the corresponding end-to-end channel (summed over all ν and weighted with $\phi_{\mathrm{NL},\nu}^2$).

At the same time, the (system relevant) variance of the perturbation $\sigma_{\Delta\boldsymbol{a}}^2 \overset{\text{def}}{=} \mathrm{E}\{\,\|\Delta\boldsymbol{a}\|^2\,\}$ depends as well on the properties of the modulation format $\mathcal{A}$ which in turn is a problem addressed by the extended Gaussian noise (EGN)-model [34], cf. also the discussion in [5, Sec. F and Appx.]. Note, that the derivation of (49) does not require any assumptions on the signal (albeit its pulse-shape)—in particular no Gaussian assumption.

We can identify three relevant system parameters that characterize the nonlinear response: the map strength $\mathcal{S}_{T,\rho} = L_{\mathrm{eff}}/L_{\mathrm{D}}$ (or equivalently the ν-dependent $\mathcal{S}_{T,\nu} = L_{\mathrm{eff}}/L_{\mathrm{wo},\nu}$) which is a measure of the temporal extent, i.e., the memory of the nonlinear interaction. Secondly, the (ν-dependent) nonlinear phase shift $\phi_{\mathrm{NL},\nu} \overset{\text{def}}{=} \frac{8}{9}\frac{L_{\mathrm{eff}}}{L_{\mathrm{NL},\nu}}$ that depends via $L_{\mathrm{NL},\nu}$ linearly on the launch power P_ν and essentially acts as a scaling factor to the nonlinear distortion $\Delta\boldsymbol{a}[k]$. And at last, the total kernel energy $E_{h,\nu}$ which charactarizes the strength of the nonlinear interaction—independent of the launch power.

E. Application to Fiber Nonlinearity Compensation

The derived channel models also find applications to fiber nonlinearity compensation where implementation complexity is of particular interest. An experimental demonstration of intra-channel fiber nonlinearity compensation based on the

[12]In (49) the common pre-factor $(\frac{8}{9}\frac{L_{\mathrm{eff}}}{L_{\mathrm{NL},\nu}})^2$ is omitted here and the energy in time- and frequency-domain is calculated over the whole support of the probe and interfering wavelength channel, whereas [27, Eq. (1)] is evaluated only at a single frequency ω. Beyond that, to include all SCI and XCI contributions one needs to sum over all ν—the GN-model in its standard form also includes MCI.

time-domain model in (38) has been presented in [35]. In terms of computational efficiency a frequency-domain implementation can be superior to the time-domain implementation, in particular, for cases where the number of nonlinear interacting pulses is large.

This is typically the case for large map strengths $\mathcal{S}_{T,\rho}$, large relative frequency offsets $\Delta\omega_\nu$, i.e., large $\mathcal{S}_{T,\nu}$, and pulse shapes $h_{\mathrm{T}}(t)$ that extend over multiple symbol durations, e.g., a root-raised cosine (RRC) shape with small roll-off factor ρ. Then, the number of coefficients of the time-domain kernel $h_\nu[\boldsymbol{\kappa}]$ exceeding a relevant energy level grows very rapidly leading to a large number of multiplications and summations. The frequency-domain picture comprises only a double integral instead of a triple sum and can be efficiently implemented using standard signal processing techniques.

Algorithm 1: REG-PERT-FD for the SCI contribution

1 $\boldsymbol{a}_\lambda[k] = \mathrm{overlapSaveSplit}(\langle\, \boldsymbol{a}[k] \,\rangle, N_{\mathrm{DFT}}, K)$
2 $k, \mu, \mu_1, \mu_2 \in \{\, 0, 1, \ldots, N_{\mathrm{DFT}} - 1 \,\}$
3 $H_\rho[\mu_1, \mu_2, \mu_3] = H_\rho[\boldsymbol{\mu}] = H_\rho(\mathrm{e}^{\mathrm{j}\frac{2\pi}{N_{\mathrm{DFT}}}\boldsymbol{\mu}})$
4 **forall** λ **do**
5 $\boldsymbol{A}_\lambda[\mu] = \mathrm{DFT}\{\, \boldsymbol{a}_\lambda[k] \,\}$
6 **forall** μ **do**
7 $\mu_3 = \mathrm{mod}_{N_{\mathrm{DFT}}}(\mu - \mu_1 + \mu_2)$
8 $\Delta\boldsymbol{A}_\lambda^{\mathrm{SCI}}[\mu] = -\mathrm{j}\frac{\phi_{\mathrm{NL},\rho}}{N_{\mathrm{DFT}}^2}$ $\times \sum_{\mu_1,\mu_2} \boldsymbol{A}_\lambda[\mu_1]\boldsymbol{A}_\lambda^{\mathsf{H}}[\mu_2]\boldsymbol{A}_\lambda[\mu_3]H_\rho[\mu_1,\mu_2,\mu_3]$
9 $\boldsymbol{Y}_\lambda^{\mathrm{PERT}}[\mu] = \boldsymbol{A}_\lambda[\mu] + \Delta\boldsymbol{A}_\lambda^{\mathrm{SCI}}[\mu]$
10 **end**
11 $\boldsymbol{y}_\lambda^{\mathrm{PERT}}[k] = \mathrm{DFT}^{-1}\{\, \boldsymbol{Y}_\lambda^{\mathrm{PERT}}[\mu] \,\}$
12 **end**
13 $\langle \boldsymbol{y}^{\mathrm{PERT}}[k] \rangle = \mathrm{overlapSaveAppend}(\boldsymbol{y}_\lambda^{\mathrm{PERT}}[k], N_{\mathrm{DFT}}, K)$

Exemplarily for the SCI contribution, Algorithm 1 realizes the regular perturbation (REG-PERT) procedure in $1/T$-periodic *discrete* frequency-domain (FD) corresponding to the continuous-frequency relation in (37). Here, the overlap-save algorithm is used to split the sequence $\langle\, \boldsymbol{a}[k] \,\rangle$ into overlapping blocks $\boldsymbol{a}_\lambda[k] \circ\!\!-\!\!\bullet\, \boldsymbol{A}_\lambda[\mu]$ of size N_{DFT} enumerated by the subindex $\lambda \in \mathbb{N}$ [36]. The block size is equal to the size of the discrete Fourier transform (DFT)[13] and the overlap between successive blocks is K. The *aliased* frequency-domain kernel is discretized to obtain the coefficients

$$H_\rho[\mu_1, \mu_2, \mu_3] = H_\rho[\boldsymbol{\mu}] \overset{\text{def}}{=} H_\rho(\mathrm{e}^{\mathrm{j}\frac{2\pi}{N_{\mathrm{DFT}}}\boldsymbol{\mu}}) \tag{50}$$

where N_{DFT} is the number of discrete-frequency samples per dimension[14]. The discrete-frequency indices μ_1 and μ_2 are elements of the set $\{\, 0, 1, \ldots, N_{\mathrm{DFT}} - 1 \,\}$ whereas μ_3 must be (modulo) reduced to the same number set due to the $1/T$-periodicity of ω_3 in (37). The number of coefficients can be decreased by pruning, similar to techniques already applied to VSTF models [37]. However, note that in contrast to VSTF models the proposed algorithm operates on the $1/T$-periodic spectrum of blocks of transmit symbols $\boldsymbol{a}_\lambda[k]$ and the filter coefficients are taken from the *aliased* frequency-domain kernel which also includes the matched filter on the receiver-side. Line 8 of the algorithm effectively realizes equation (37) where the (double) sum is performed over all μ_1 and μ_2. After frequency-domain processing the blocks of *perturbed* receive symbols $\boldsymbol{Y}_\lambda^{\mathrm{PERT}}[\mu] \bullet\!\!-\!\!\circ\, \boldsymbol{y}_\lambda^{\mathrm{PERT}}[k]$ are transformed back to time-domain where the $N_{\mathrm{DFT}} - K$ desired output symbols of each block are *appended* to obtain the perturbed sequence $\langle\, \boldsymbol{y}^{\mathrm{PERT}}[k] \,\rangle$. Algorithm 1 can be straightforwardly generalized to XCI analogously to (46).

The time- and frequency-domain picture of the *regular* perturbation approach are equivalent due to the DTFT in (37), (38) which interrelates both representations. Algorithm 1 represents a practical realization in discrete-frequency which produces the same (numerical) results as the discrete-time model as long as N_{DFT} and K are chosen sufficiently large for a given system scenario. To that end, Section IV will compare the regular discrete-time and -frequency model to the reference channel model implemented via the SSFM. In the next section, the regular model is extended to a combined regular-logarithmic model where a subset of the perturbations are considered as multiplicative, i.e., perturbations that cause a rotation in *phase* or in the *state of polarization* (SOP).

F. Regular-Logarithmic Model in Discrete-Time Domain

It was already noted in [38] that the regular VSTF approach (or the equivalent RP method) in (26) reveals an energy-divergence problem if the optical launch power P is too high—or more precisely if the nonlinear phase shift ϕ_{NL} is too large. Using a first-order RP approach, a pure phase rotation is approximated by $\exp(\mathrm{j}\phi) \approx 1 + \mathrm{j}\phi$. While multiplication with $\exp(\mathrm{j}\phi)$ is an energy conserving transformation (i.e., the

[13]The one-dimensional DFT is performed on each vector component of $\boldsymbol{a}_\lambda[k]$ and always relates the *whole* blocks of length N_{DFT}.

[14]Note, that the frequency discretization of the kernel must not necessarily coincide with the transformation length N_{DFT}.

$$\Delta\boldsymbol{A}^{\mathrm{SCI}}(\mathrm{e}^{\mathrm{j}\omega T}) = \frac{T}{E_{\mathrm{T}}}\mathrm{ALIAS}\{\, \Delta\boldsymbol{S}^{\mathrm{SCI}}(\omega)\cdot H_{\mathrm{T}}^*(\omega) \,\} = -\mathrm{j}\underbrace{\frac{8}{9}\frac{L_{\mathrm{eff}}}{L_{\mathrm{NL},\rho}}}_{\phi_{\mathrm{NL},\rho}}\frac{T^2}{(2\pi)^2}\int_{\mathbb{T}^2}\boldsymbol{A}(\mathrm{e}^{\mathrm{j}\omega_1 T})\boldsymbol{A}^{\mathsf{H}}(\mathrm{e}^{\mathrm{j}\omega_2 T})\boldsymbol{A}(\underbrace{\mathrm{e}^{\mathrm{j}\omega_3 T}}_{\omega_3=\mathrm{FOLD}\{\,\omega-\omega_1+\omega_2\,\}\in\mathbb{T}})H_\rho(\mathrm{e}^{\mathrm{j}\boldsymbol{\omega}T})\,\mathrm{d}^2\boldsymbol{\omega} \tag{37}$$

$$\Delta\boldsymbol{a}^{\mathrm{SCI}}[k] = \frac{T}{E_{\mathrm{T}}}\Delta\boldsymbol{s}^{\mathrm{SCI}}(t) * h_{\mathrm{T}}^*(-t)\Big|_{t=kT} = -\mathrm{j}\frac{8}{9}\frac{L_{\mathrm{eff}}}{L_{\mathrm{NL},\rho}}\sum_{\boldsymbol{\kappa}\in\mathbb{Z}^3}\boldsymbol{a}[k+\kappa_1]\boldsymbol{a}^{\mathsf{H}}[k+\kappa_2]\boldsymbol{a}[k+\kappa_3]h_\rho[\boldsymbol{\kappa}] \tag{38}$$

$\hat{\mathcal{F}}_{\boldsymbol{\kappa}\leftrightarrow\boldsymbol{\omega}}\{\,\cdot\,\}$

norm is invariant under phase rotation), the RP approximation is obviously *not* energy conserving. In the context of optical transmission, already a trivial (time-constant) average phase rotation due nonlinear interaction is not well modeled by the RP method.

This inconsistency was first addressed in the early 2000s [4], [39] and years later revived in the context of intra-channel fiber nonlinearity mitigation. E.g. in [40], [41] it turned out that a certain subset of symbol combinations in the time-domain RP model deterministically creates a perturbation oriented into the $-$j-direction from the transmit symbol $\boldsymbol{a}[k]$. Similarly, in the pulse-collision picture [11]–[13] a subset of degenerate[15] cross-channel pulse collisions were properly associated to distortions exhibiting a *multiplicative* nature. In the same series of contributions, these subsets of degenerate distortions were first termed *two-* and *three-pulse collisions*, i.e., symbol combinations $\boldsymbol{\kappa} \in \mathbb{Z}^3$ in (47) with $\kappa_3 = 0$ in our terminology. While the pulse collision picture covers only cross-channel effects, we will extent the analysis also to intra-channel effects.

In this context, we review some properties of the kernel coefficients relevant for inter-channel ($\nu \neq \rho$) two- and three-pulse collisions [13]

$$h_\nu[\kappa_1, \kappa_2, 0] \in \mathbb{R}, \qquad \text{if } \kappa_1 = \kappa_2 \tag{51}$$

$$h_\nu[\kappa_1, \kappa_2, 0] = h_\nu^*[\kappa_2, \kappa_1, 0] \in \mathbb{C} \qquad \text{if } \kappa_1 \neq \kappa_2, \tag{52}$$

where two-pulse collisions with $\kappa_1 = \kappa_2$ in (51) are doubly degenerate and the kernel is real-valued[16]. In case of three-pulse collisions, the kernel is generally complex-valued but due to its symmetry property in (52) and the double sum over all (nonzero) pairs of $[\kappa_1, \kappa_2]^{\mathsf{T}}$ in (47) the overall effect is still multiplicative.

Additionally, for intra-channel contributions ($\nu = \rho$) we find the following symmetry properties of the kernel

$$h_\rho[\kappa_1, \kappa_2, \kappa_3] = h_\rho[\kappa_3, \kappa_2, \kappa_1] \tag{53}$$

$$h_\rho[\kappa_1, \kappa_2, \kappa_3] = h_\rho[-\kappa_1, -\kappa_2, -\kappa_3], \tag{54}$$

and we identify a second degenerate case with $\kappa_1 = 0$ as source for multiplicative distortions, cf. the symmetric form of (38) w.r.t. κ_1 and κ_3.

In the following, the original RP solution is modified such that perturbations originating from certain degenerate mixing products are associated with a multiplicative perturbation. Similar to [13], [41], [42], we extend the previous RP model to a combined regular-logarithmic model. It takes the general form of

$$\boldsymbol{y}[k] = \exp\left(\mathrm{j}\Phi[k] + \mathrm{j}\vec{\boldsymbol{s}}[k] \cdot \vec{\boldsymbol{\sigma}}\right) \left(\boldsymbol{a}[k] + \Delta\boldsymbol{a}[k]\right). \tag{55}$$

In addition to the regular, additive perturbation $\Delta\boldsymbol{a}[k]$ we now also consider a *phase* rotation by $\exp(\mathrm{j}\Phi[k])$ and a rotation in the *state of polarization* by $\exp(\mathrm{j}\vec{\boldsymbol{s}}[k] \cdot \vec{\boldsymbol{\sigma}})$. Here, $\exp(\cdot)$ denotes the *matrix exponential*. All perturbative terms combine both SCI and XCI effects, i.e., the *additive* perturbation $\Delta\boldsymbol{a}[k] \in \mathbb{C}^2$ is the sum of SCI and XCI contributions. The *time-dependent* phase rotation is given by $\exp(\mathrm{j}\Phi[k])$ with the diagonal matrix $\Phi[k] \in \mathbb{R}^{2\times 2}$ defined as

$$\Phi[k] \triangleq \phi^{\mathrm{SCI}}[k]\,\mathbf{I} + \phi^{\mathrm{XCI}}[k]\,\mathbf{I}, \tag{56}$$

i.e., we find a *common* phase term for both polarizations originating from intra- and inter-channel effects.

The combined effect of intra- and inter-channel cross-polarization modulation (XPolM) is expressed by the *Pauli matrix expansion* $\vec{\boldsymbol{s}}[k] \cdot \vec{\boldsymbol{\sigma}} \in \mathbb{C}^{2\times 2}$ using (6), with the notation adopted from [20] and [43]. The expansion defines a unitary rotation in Jones space of the perturbed vector $\boldsymbol{a}[k] + \Delta\boldsymbol{a}[k]$ around the *time-dependent* Stokes vector $\vec{\boldsymbol{s}}[k]$ and is explained in more detail in the subsequent subsection.

1) SCI Contribution: To discuss the SCI contribution we first introduce the following symbol sets

$$\mathcal{K}^{\mathrm{SCI}} = \{\, [\kappa_1, \kappa_2, \kappa_3]^{\mathsf{T}} \in \mathbb{Z}^3 \mid |h_\rho[\boldsymbol{\kappa}]/h_\rho[\mathbf{0}]|^2 > \Gamma^{\mathrm{SCI}} \,\} \tag{57}$$

$$\mathcal{K}_\phi^{\oplus} \triangleq \{\, \mathcal{K}^{\mathrm{SCI}} \mid \kappa_1 = 0 \wedge \kappa_2 \neq 0 \wedge \kappa_3 \neq 0 \,\} \tag{58}$$

$$\mathcal{K}_\phi^{\ominus} \triangleq \{\, \mathcal{K}^{\mathrm{SCI}} \mid \kappa_3 = 0 \wedge \kappa_2 \neq 0 \wedge \kappa_1 \neq 0 \,\} \tag{59}$$

$$\mathcal{K}_\phi^{\mathrm{SCI}} \triangleq \mathcal{K}_\phi^{\oplus} \cap \mathcal{K}_\phi^{\ominus} \cap \{\, \boldsymbol{\kappa} = \mathbf{0} \,\} \tag{60}$$

$$\mathcal{K}_\Delta^{\mathrm{SCI}} \triangleq \mathcal{K}^{\mathrm{SCI}} \setminus \mathcal{K}_\phi^{\mathrm{SCI}}, \tag{61}$$

where (57) defines the *base* set including all possible symbol combinations that exceed a certain energy level Γ^{SCI} normalized to the energy of the *center* tap at $\boldsymbol{\kappa} = \mathbf{0}$. In (58), (59) the joint set of degenerate two- and three-pulse collisions for SCI are defined which follow directly from the kernel properties in (51), (52) for $\kappa_3 = 0$, and (53), (54) for $\kappa_1 = 0$. The set of indices for *multiplicative* distortions $\mathcal{K}_\phi^{\mathrm{SCI}}$ in (60) also includes the singular case $\boldsymbol{\kappa} = \mathbf{0}$. Then, the additive set is simply the complementary set of $\mathcal{K}_\phi^{\mathrm{SCI}}$ w.r.t. the base set $\mathcal{K}^{\mathrm{SCI}}$.

We start with the additive perturbation from the previous section in (38) which now reads

$$\Delta\boldsymbol{a}^{\mathrm{SCI}}[k] = -\mathrm{j}\phi_{\mathrm{NL},\rho} \sum_{\mathcal{K}_\Delta^{\mathrm{SCI}}} \boldsymbol{a}[k+\kappa_1]\boldsymbol{a}^{\mathsf{H}}[k+\kappa_2]\boldsymbol{a}[k+\kappa_3]h_\rho[\boldsymbol{\kappa}], \tag{62}$$

where the triple sum is now restricted to the set $\mathcal{K}_\Delta^{\mathrm{SCI}}$ excluding all combinations which result in a multiplicative distortion, cf. (61).

To calculate the common phase $\phi^{\mathrm{SCI}}[k]$ and the intra-channel Stokes rotation vector $\vec{\boldsymbol{s}}^{\,\mathrm{SCI}}[k]$ we first analyse the expression $\boldsymbol{a}[k+\kappa_1]\boldsymbol{a}^{\mathsf{H}}[k+\kappa_2]\boldsymbol{a}[k+\kappa_3]$ from the original equation in (38). For the set $\mathcal{K}_\phi^{\oplus}$ with $\kappa_1 = 0$ the triple product factors into the respective transmit symbol $\boldsymbol{a}[k]$ and a scalar value $\boldsymbol{a}^{\mathsf{H}}[k+\kappa_2]\boldsymbol{a}[k+\kappa_3]$. After multiplication with $h_\rho[0, \kappa_2, \kappa_3]$ and summation of all $\boldsymbol{\kappa} \in \mathcal{K}_\phi^{\oplus}$ the perturbation is strictly imaginary-valued (cf. symmetry properties in (53), (54)).

On the other hand, for $\mathcal{K}_\phi^{\ominus}$ with $\kappa_3 = 0$ we have to rearrange the triple product using the matrix expansion from (7) to factor the expression accordingly as[17]

$$\boldsymbol{a}\boldsymbol{a}^{\mathsf{H}}\boldsymbol{a} = \frac{1}{2}\left(\boldsymbol{a}^{\mathsf{H}}\boldsymbol{a}\,\mathbf{I} + (\boldsymbol{a}^{\mathsf{H}}\vec{\boldsymbol{\sigma}}\boldsymbol{a}) \cdot \vec{\boldsymbol{\sigma}}\right)\boldsymbol{a}. \tag{63}$$

The first term $\boldsymbol{a}^{\mathsf{H}}\boldsymbol{a}\,\mathbf{I}$ also contributes to a common phase term, whereas the second term $(\boldsymbol{a}^{\mathsf{H}}\vec{\boldsymbol{\sigma}}\boldsymbol{a}) \cdot \vec{\boldsymbol{\sigma}} \in \mathbb{C}^{2\times 2}$ is a traceless and

[15] in the sense that not all four interacting pulses are distinct.

[16] The transmit pulse-shape $h_{\mathrm{T}}(t)$ is assumed to be a real-valued (root) raised-cosine.

[17] multiplication with $h_\rho[\boldsymbol{\kappa}]$ and summation over $\boldsymbol{\kappa} \in \mathcal{K}_\phi^{\mathrm{SCI}}$ are implied.

Hermitian matrix s.t. $\exp(\mathrm{j}(\boldsymbol{a}^{\mathsf{H}}\vec{\boldsymbol{\sigma}}\boldsymbol{a})\cdot\vec{\boldsymbol{\sigma}})$ is a unitary polarization rotation[18].

The multiplicative perturbation $\exp(\mathrm{j}\phi^{\mathrm{SCI}}[k])$ with $\phi^{\mathrm{SCI}}[k] \in \mathbb{R}$ is then given by

$$\begin{aligned}\phi^{\mathrm{SCI}}[k] =& -\phi_{\mathrm{NL},\rho}\sum_{\mathcal{K}_\phi^{\oplus}}\boldsymbol{a}^{\mathsf{H}}[k+\kappa_2]\boldsymbol{a}[k+\kappa_3]h_\rho[\boldsymbol{\kappa}]\\ &-\frac{1}{2}\phi_{\mathrm{NL},\rho}\sum_{\mathcal{K}_\phi^{\ominus}}\boldsymbol{a}^{\mathsf{H}}[k+\kappa_2]\boldsymbol{a}[k+\kappa_1]h_\rho[\boldsymbol{\kappa}]\\ &-\phi_{\mathrm{NL},\rho}\left\|\boldsymbol{a}[k]\right\|^2 h_\rho[\boldsymbol{0}] \qquad (64)\\ =& -\frac{3}{2}\phi_{\mathrm{NL},\rho}\sum_{\mathcal{K}_\phi^{\ominus}}\boldsymbol{a}^{\mathsf{H}}[k+\kappa_2]\boldsymbol{a}[k+\kappa_1]h_\rho[\boldsymbol{\kappa}]\\ &-\phi_{\mathrm{NL},\rho}\left\|\boldsymbol{a}[k]\right\|^2 h_\rho[\boldsymbol{0}]. \qquad (65)\end{aligned}$$

Given a wide-sense stationary transmit sequence $\langle\,\boldsymbol{a}[k]\,\rangle$, the induced nonlinear phase shift has a *time-average* value $\bar{\phi}^{\mathrm{SCI}}$, around which the instantaneous phase $\phi^{\mathrm{SCI}}[k]$ may fluctuate (cf. also [44]).

The instantaneous rotation of the SOP due to the expression $\exp(\mathrm{j}\vec{\boldsymbol{s}}^{\,\mathrm{SCI}}[k]\cdot\vec{\boldsymbol{\sigma}}) \in \mathbb{C}^{2\times 2}$ causes intra-channel XPolM [45]. It is given by

$$\begin{aligned}\vec{\boldsymbol{s}}^{\,\mathrm{SCI}}[k]\cdot\vec{\boldsymbol{\sigma}} =& -\frac{1}{2}\phi_{\mathrm{NL},\rho}\sum_{\mathcal{K}_\phi^{\ominus}}\Big(2\,\boldsymbol{a}[k+\kappa_1]\boldsymbol{a}^{\mathsf{H}}[k+\kappa_2]\\ &-\boldsymbol{a}^{\mathsf{H}}[k+\kappa_2]\boldsymbol{a}[k+\kappa_1]\mathbf{I}\Big)h_\rho[\boldsymbol{\kappa}], \qquad (66)\end{aligned}$$

where we made use of the relation in (6). The rotation matrix $\exp(\mathrm{j}\vec{\boldsymbol{s}}^{\,\mathrm{SCI}}[k]\cdot\vec{\boldsymbol{\sigma}})$ is unitary and $\vec{\boldsymbol{s}}^{\,\mathrm{SCI}}[k]\cdot\vec{\boldsymbol{\sigma}}$ is Hermitian and traceless. The physical meaning of the transformation described in (66) is as follows: The perturbed transmit vector $(\boldsymbol{a}[k]+\Delta\boldsymbol{a}[k])$ in (55) is transformed into the polarization eigenstate $\vec{\boldsymbol{s}}^{\,\mathrm{SCI}}[k]$ (i.e., into the basis defined by the eigenvectors of $\vec{\boldsymbol{s}}^{\,\mathrm{SCI}}[k]\cdot\vec{\boldsymbol{\sigma}}$). There, both vector components receive equal but opposite phase shifts and the result is transformed back to the x/y-basis of the transmit vector. In Stokes space, the operation can be understood as a precession of $(\vec{\boldsymbol{a}}[k]+\Delta\vec{\boldsymbol{a}}[k])$ around the Stokes vector $\vec{\boldsymbol{s}}^{\,\mathrm{SCI}}[k]$ by an angle equal to its length $\left\|\vec{\boldsymbol{s}}^{\,\mathrm{SCI}}[k]\right\|$. The intra-channel Stokes vector $\vec{\boldsymbol{s}}^{\,\mathrm{SCI}}[k]$ depends via the nonlinear kernel $h_\rho[\boldsymbol{\kappa}]$ on the transmit symbols within the memory of the nonlinear interaction $\mathcal{S}_{T,\rho}$ around $\boldsymbol{a}[k]$. Similar to the nonlinear phase shift—for a wide-sense stationary input sequence—the Stokes vector $\vec{\boldsymbol{s}}^{\,\mathrm{SCI}}[k]$ has a time-constant average value around which it fluctuates over time.

2) XCI Contribution: The same methodology is now applied to cross-channel effects. The symbol set definitions for XCI follow from the considerations in the previous section.

$$\mathcal{K}_\nu^{\mathrm{XCI}} = \{\,[\kappa_1,\kappa_2,\kappa_3]^{\mathsf{T}} \in \mathbb{Z}^3 \mid |h_\nu[\boldsymbol{\kappa}]/h_\nu[\boldsymbol{0}]|^2 > \Gamma_\nu^{\mathrm{XCI}}\,\} \quad (67)$$

$$\begin{aligned}\mathcal{K}_{\phi,\nu}^{\mathrm{XCI}} \overset{\text{def}}{=}& \{\,\mathcal{K}_\nu^{\mathrm{XCI}} \mid \kappa_3 = 0 \wedge \kappa_2 \neq 0 \wedge \kappa_1 \neq 0\,\}\\ &\cap\{\,\boldsymbol{\kappa} = \boldsymbol{0}\,\} \qquad (68)\end{aligned}$$

$$\mathcal{K}_{\Delta,\nu}^{\mathrm{XCI}} \overset{\text{def}}{=} \mathcal{K}_\nu^{\mathrm{XCI}} \setminus \mathcal{K}_{\phi,\nu}^{\mathrm{XCI}}, \qquad (69)$$

[18]Since the Pauli expansion $\vec{\boldsymbol{u}}\cdot\vec{\boldsymbol{\sigma}}$ in (6) is Hermitian, the expression $\exp(\mathrm{j}\,\vec{\boldsymbol{u}}\cdot\vec{\boldsymbol{\sigma}})$ is unitary.

where the subscript ν indicates the channel number of the respective interfering channel. For $\mathcal{K}_{\phi,\nu}^{\mathrm{XCI}}$, only the degenerate case $\kappa_3 = 0$ has to be considered[19]. Similar to (63), the expression $\boldsymbol{b}\boldsymbol{b}^{\mathsf{H}} + \boldsymbol{b}^{\mathsf{H}}\boldsymbol{b}\,\mathbf{I}$ from (47) is rearranged to obtain

$$\underbrace{\frac{3}{2}\begin{bmatrix} b_{\mathsf{x}}b_{\mathsf{x}}^*+b_{\mathsf{y}}b_{\mathsf{y}}^* & 0\\ 0 & b_{\mathsf{y}}b_{\mathsf{y}}^*+b_{\mathsf{x}}b_{\mathsf{x}}^*\end{bmatrix}}_{\boldsymbol{b}^{\mathsf{H}}\boldsymbol{b}\,\mathbf{I}} + \underbrace{\frac{1}{2}\begin{bmatrix} b_{\mathsf{x}}b_{\mathsf{x}}^*-b_{\mathsf{y}}b_{\mathsf{y}}^* & 2b_{\mathsf{x}}b_{\mathsf{y}}^*\\ 2b_{\mathsf{y}}b_{\mathsf{x}}^* & b_{\mathsf{y}}b_{\mathsf{y}}^*-b_{\mathsf{x}}b_{\mathsf{x}}^*\end{bmatrix}}_{2\,\boldsymbol{b}\boldsymbol{b}^{\mathsf{H}}-\boldsymbol{b}^{\mathsf{H}}\boldsymbol{b}\,\mathbf{I}\,=\,(\boldsymbol{b}^{\mathsf{H}}\vec{\boldsymbol{\sigma}}\boldsymbol{b})\cdot\vec{\boldsymbol{\sigma}}}, \quad (70)$$

where the argument and subscript ν is omitted for concise notation. The multiplicative cross-channel contribution is again split into a common phase shift in both polarizations and an equal but opposite phase shift in the basis given by the instantaneous Stokes vector of the νth interferer.

We define the total, common phase shift due to cross-channel interference as

$$\phi^{\mathrm{XCI}}[k] = -\sum_{\nu\neq\rho}\frac{3}{2}\phi_{\mathrm{NL},\nu}\sum_{\mathcal{K}_{\phi,\nu}^{\mathrm{XCI}}}\boldsymbol{b}_\nu^{\mathsf{H}}[k+\kappa_1]\boldsymbol{b}_\nu[k+\kappa_2]\;h_\nu[\boldsymbol{\kappa}] \quad (71)$$

which depends on the instantaneous sum over all interfering channels and the sum of $\boldsymbol{b}_\nu^{\mathsf{H}}\boldsymbol{b}_\nu$ over $[\kappa_1,\kappa_2]^{\mathsf{T}}$. The effective, instantaneous cross-channel Stokes vector $\vec{\boldsymbol{s}}^{\,\mathrm{XCI}}[k]$ is given by

$$\begin{aligned}\vec{\boldsymbol{s}}^{\,\mathrm{XCI}}[k]\cdot\vec{\boldsymbol{\sigma}} =& -\sum_{\nu\neq\rho}\frac{1}{2}\phi_{\mathrm{NL},\nu}\sum_{\mathcal{K}_{\phi,\nu}^{\mathrm{XCI}}}\Big(2\,\boldsymbol{b}_\nu[k+\kappa_1]\boldsymbol{b}_\nu^{\mathsf{H}}[k+\kappa_2]\\ &-\boldsymbol{b}_\nu^{\mathsf{H}}[k+\kappa_2]\boldsymbol{b}_\nu[k+\kappa_1]\mathbf{I}\Big)h_\nu[\boldsymbol{\kappa}]. \qquad (72)\end{aligned}$$

Note, that the expressions in (71), (72) include both contributions from two- and three pulse collisions (cf. [13, Eq. (10)–(13)]).

3) Energy of Coefficients in Discrete-Time Domain: The energy of the kernel coefficients is defined for the subsets given in (57)–(61). We find for the different symbol sets

$$E_h^{\mathrm{SCI}} \overset{\text{def}}{=} \sum_{\mathcal{K}^{\mathrm{SCI}}}|h_\rho[\boldsymbol{\kappa}]|^2 \quad (73)$$

$$E_{h,\Delta}^{\mathrm{SCI}} \overset{\text{def}}{=} \sum_{\mathcal{K}_\Delta^{\mathrm{SCI}}}|h_\rho[\boldsymbol{\kappa}]|^2 \quad (74)$$

$$E_{h,\phi}^{\mathrm{SCI}} \overset{\text{def}}{=} \sum_{\mathcal{K}_\phi^{\mathrm{SCI}}}|h_\rho[\boldsymbol{\kappa}]|^2, \quad (75)$$

with the clipping factor Γ^{SCI} in (57) equal to zero. The energy for cross-channel effects is defined accordingly with the sets from (67)–(69). Since the subsets for additive and multiplicative effects are always disjoint we have $E_h^{\mathrm{SCI}} = E_{h,\Delta}^{\mathrm{SCI}} + E_{h,\phi}^{\mathrm{SCI}}$.

G. Regular-Logarithmic Model in Frequency-Domain

Similar to the previous section, we first review some kernel properties of the aliased frequency-domain kernel

$$H_\nu(\mathrm{e}^{\mathrm{j}\boldsymbol{\omega}T}) \in \mathbb{R}, \quad \text{if } \omega_2=\omega_1 \Leftrightarrow \omega_3=\omega \Leftrightarrow \upsilon_2 = 0, \quad (76)$$

$$\begin{aligned}H_\rho(\mathrm{e}^{\mathrm{j}\boldsymbol{\omega}T}) \in \mathbb{R}, \quad &\text{if } \omega_2=\omega_1 \Leftrightarrow \omega_3=\omega \Leftrightarrow \upsilon_2 = 0 \qquad (77)\\ &\vee\ \omega_2=\omega_3 \Leftrightarrow \omega_1=\omega \Leftrightarrow \upsilon_1 = 0,\end{aligned}$$

where the two (doubly) degenerate cases $\omega_1 = \omega_2$ and $\omega_3 = \omega_2$ correspond to classical inter- and intra-channel cross-phase

[19]due to the kernel properties of $h_\nu[\kappa_1,\kappa_2,0]$ in (51), (52).

modulation (XPM). For the special case that the transmit pulse $h_{\mathrm{T}}(t)$ has a RRC shape with roll-off factor $\rho = 0$, we find that the kernel takes the value 1 independent of $\boldsymbol{\omega}$ in (76), (77). This result is used in the remainder to simplify the expression for the average phase- and polarization rotation.

The frequency-domain model is now modified such that the degenerate contributions will be associated with multiplicative distortions. Due to the multiplicative nature, average effects can be straightforwardly incorporated into the frequency-domain model as they are both treated as constant pre-factors in the time- and frequency-domain representation. We will see in the next section that this already leads to significantly improved results compared to the regular model. Note that, in contrast to the regular models, the regular-logarithmic model in time and frequency are no longer equivalent.

The general form of the combined regular-logarithmic model in frequency is given by

$$\begin{aligned}\boldsymbol{Y}(\mathrm{e}^{\mathrm{j}\omega T}) = \exp\left(\mathrm{j}\bar{\Phi} + \mathrm{j}\vec{\boldsymbol{S}}\cdot\vec{\boldsymbol{\sigma}}\right) \\ \times \left(\boldsymbol{A}(\mathrm{e}^{\mathrm{j}\omega T}) + \Delta\boldsymbol{A}(\mathrm{e}^{\mathrm{j}\omega T})\right),\end{aligned} \tag{78}$$

where the phase- and polarization-term take on a *frequency*-constant value, i.e., independent of $\mathrm{e}^{\mathrm{j}\omega T}$ (and vice-versa independent of k in the time-domain picture). Following the same terminology as before, we introduce the *average* multiplicative perturbation of the common phase term

$$\bar{\Phi} \overset{\text{def}}{=} \bar{\phi}^{\mathrm{SCI}}\,\mathbf{I} + \bar{\phi}^{\mathrm{XCI}}\,\mathbf{I}, \tag{79}$$

as the sum of the intra-channel contribution $\bar{\phi}^{\mathrm{SCI}} \in \mathbb{R}$ and the inter-channel contribution $\bar{\phi}^{\mathrm{XCI}} \in \mathbb{R}$. Similarly, for the *average* polarization rotation we have

$$\vec{\boldsymbol{S}}\cdot\vec{\boldsymbol{\sigma}} \overset{\text{def}}{=} \vec{\boldsymbol{S}}^{\,\mathrm{SCI}}\cdot\vec{\boldsymbol{\sigma}} + \vec{\boldsymbol{S}}^{\,\mathrm{XCI}}\cdot\vec{\boldsymbol{\sigma}}, \tag{80}$$

where $\vec{\boldsymbol{S}}\cdot\vec{\boldsymbol{\sigma}}$ is again Hermitian and traceless, which in turn makes the matrix exponential $\exp(\mathrm{j}\vec{\boldsymbol{S}}\cdot\vec{\boldsymbol{\sigma}})$ unitary.

1) SCI Contribution: The two degenerate frequency conditions in (77) are used in the expression (37) to obtain the *average*, intra-channel phase distortion. To that end, the triple product $\boldsymbol{A}\boldsymbol{A}^{\mathsf{H}}\boldsymbol{A}$ in (37) is rearranged similar to (63). First, the general *frequency-dependent* expression $\phi^{\mathrm{SCI}}(\mathrm{e}^{\mathrm{j}\omega T})$ is given by

$$\begin{aligned}\phi^{\mathrm{SCI}} = -\quad & \phi_{\mathrm{NL},\rho}\frac{T}{(2\pi)^2}\int_{\mathbb{T}}\left\|\boldsymbol{A}(\mathrm{e}^{\mathrm{j}\omega_2 T})\right\|^2 H_{\rho}(\mathrm{e}^{\mathrm{j}[\omega,\omega_2,\omega_2]^{\mathsf{T}}T})\mathrm{d}\omega_2 \\ & -\frac{1}{2}\phi_{\mathrm{NL},\rho}\frac{T}{(2\pi)^2}\int_{\mathbb{T}}\left\|\boldsymbol{A}(\mathrm{e}^{\mathrm{j}\omega_1 T})\right\|^2 H_{\rho}(\mathrm{e}^{\mathrm{j}[\omega_1,\omega_1,\omega]^{\mathsf{T}}T})\mathrm{d}\omega_1,\end{aligned} \tag{81}$$

where the first term on the right-hand side in (81) corresponds to the degeneracy $\omega_2 = \omega_3 \Leftrightarrow \omega_1 = \omega$ and the second term corresponds to $\omega_2 = \omega_1 \Leftrightarrow \omega_3 = \omega$. We simplify the expression using the RRC $\rho = 0$ approximation to obtain the average, intra-channel phase distortion

$$\bar{\phi}^{\mathrm{SCI}} = -\frac{3}{2}\phi_{\mathrm{NL},\rho}\frac{T}{(2\pi)^2}\int_{\mathbb{T}}\left\|\boldsymbol{A}(\mathrm{e}^{\mathrm{j}\omega T})\right\|^2\,\mathrm{d}\omega, \tag{82}$$

which does no longer depend on the power or dispersion profile of the transmission link (given a fixed L_{eff}).

Similarly, the average intra-channel XPolM contribution can be simplified to

$$\begin{aligned}\vec{\boldsymbol{S}}^{\,\mathrm{SCI}}\cdot\vec{\boldsymbol{\sigma}} = -\frac{1}{2}\phi_{\mathrm{NL},\rho}\frac{T}{(2\pi)^2}\int_{\mathbb{T}}\Big(2\,\boldsymbol{A}(\mathrm{e}^{\mathrm{j}\omega T})\boldsymbol{A}^{\mathsf{H}}(\mathrm{e}^{\mathrm{j}\omega T}) \\ -\boldsymbol{A}^{\mathsf{H}}(\mathrm{e}^{\mathrm{j}\omega T})\boldsymbol{A}(\mathrm{e}^{\mathrm{j}\omega T})\mathbf{I}\Big)\mathrm{d}\omega.\end{aligned} \tag{83}$$

In Algorithm 2 the required modifications to the regular perturbation model (REG-PERT) are highlighted to arrive at the regular-logarithmic perturbation model (REGLOG-PERT)—again exemplarily for the SCI contribution. Lines 6,7 of Algorithm 2 translate Eq. (82), (83) to the discrete-frequency domain where the integral over all $\omega \in \mathbb{T}$ becomes a sum over all μ of the λth processing block. The average values, here, are always associated to the average values of the λth block. In Lines 10,11, the double sum to obtain $\Delta\boldsymbol{A}_{\lambda}^{\mathrm{SCI}}[\mu]$ is restricted to all combinations $\mathcal{U}$ of the discrete frequency pair $[\mu_1,\mu_2]^{\mathsf{T}}$ excluding the degenerate cases corresponding to Eq. (76), (77). The perturbed receive vector $\boldsymbol{Y}_{\lambda}^{\mathrm{PERT}}$ is then calculated according to (78) before it is transformed back to the discrete-time domain.

2) XCI Contribution: The cross-channel contributions follow from the considerations in the previous sections and we obtain for the degenerate case in (76) the total, average XCI phase shift

$$\bar{\phi}^{\mathrm{XCI}} = -\sum_{\nu\neq\rho}\frac{3}{2}\phi_{\mathrm{NL},\nu}\frac{T}{(2\pi)^2}\int_{\mathbb{T}}\left\|\boldsymbol{B}_{\nu}(\mathrm{e}^{\mathrm{j}\omega T})\right\|^2\,\mathrm{d}\omega \tag{84}$$

and analogously for the total, average XCI Stokes vector we find

$$\begin{aligned}\vec{\boldsymbol{S}}^{\,\mathrm{XCI}}\cdot\vec{\boldsymbol{\sigma}} = -\sum_{\nu\neq\rho}\frac{1}{2}\phi_{\mathrm{NL},\nu}\frac{T}{(2\pi)^2}\int_{\mathbb{T}}\Big(2\,\boldsymbol{B}_{\nu}(\mathrm{e}^{\mathrm{j}\omega T})\boldsymbol{B}_{\nu}^{\mathsf{H}}(\mathrm{e}^{\mathrm{j}\omega T}) \\ -\boldsymbol{B}_{\nu}^{\mathsf{H}}(\mathrm{e}^{\mathrm{j}\omega T})\boldsymbol{B}_{\nu}(\mathrm{e}^{\mathrm{j}\omega T})\mathbf{I}\Big)\mathrm{d}\omega.\end{aligned} \tag{85}$$

3) Energy of Coefficients in Discrete-Frequency Domain: With the notation of the discrete-frequency kernel from (50) we have according to Parseval's theorem in (49) the following definitions

$$E_{H}^{\mathrm{SCI}} \overset{\text{def}}{=} \frac{1}{N_{\mathrm{DFT}}^3}\sum_{\mathcal{U}^{\mathrm{SCI}}}|H_{\rho}[\boldsymbol{\mu}]|^2 \tag{86}$$

$$E_{H,\Delta}^{\mathrm{SCI}} \overset{\text{def}}{=} \frac{1}{N_{\mathrm{DFT}}^3}\sum_{\mathcal{U}_{\Delta}^{\mathrm{SCI}}}|H_{\rho}[\boldsymbol{\mu}]|^2 \tag{87}$$

$$E_{H,\phi}^{\mathrm{SCI}} \overset{\text{def}}{=} \frac{1}{N_{\mathrm{DFT}}^3}\sum_{\mathcal{U}_{\phi}^{\mathrm{SCI}}}|H_{\rho}[\boldsymbol{\mu}]|^2 \overset{\rho=0}{\approx} \frac{2}{N_{\mathrm{DFT}}}, \tag{88}$$

with the sets according to (77)

$$\mathcal{U}^{\mathrm{SCI}} = \{\,\boldsymbol{\mu} = [\mu_1,\mu_2,\mu_3]^{\mathsf{T}} \in \{\,0,1,\ldots,N_{\mathrm{DFT}}-1\,\}^3\,\} \tag{89}$$

$$\mathcal{U}_{\Delta}^{\mathrm{SCI}} = \{\,\mathcal{U}^{\mathrm{SCI}} \mid \mu_2 \neq \mu_1 \wedge \mu_2 \neq \mu_3\,\} \tag{90}$$

$$\mathcal{U}_{\phi}^{\mathrm{SCI}} = \{\,\mathcal{U}^{\mathrm{SCI}} \mid \mu_2 = \mu_1 \vee \mu_2 = \mu_3\,\}. \tag{91}$$

Note, that we have again $E_{H}^{\mathrm{SCI}} = E_{H,\Delta}^{\mathrm{SCI}} + E_{H,\phi}^{\mathrm{SCI}}$ and due to Parseval's theorem $E_{h}^{\mathrm{SCI}} = E_{H}^{\mathrm{SCI}}$ for $N_{\mathrm{DFT}} \to \infty$. The cardinalities of the sets are $|\mathcal{U}^{\mathrm{SCI}}| = N_{\mathrm{DFT}}^3$, $|\mathcal{U}_{\phi}^{\mathrm{SCI}}| = 2N_{\mathrm{DFT}}^2 - N_{\mathrm{DFT}}$ and $|\mathcal{U}_{\Delta}^{\mathrm{SCI}}| = |\mathcal{U}^{\mathrm{SCI}}| - |\mathcal{U}_{\phi}^{\mathrm{SCI}}|$. With the RRC pulse-shape and $\rho = 0$ we find again that $H_{\rho}(\boldsymbol{\mu}) = 1$ with

Algorithm 2: REGLOG-PERT-FD for the SCI contribution

$\boldsymbol{a}_\lambda[k] = \mathrm{overlapSaveSplit}(\langle\, \boldsymbol{a}[k] \,\rangle, N_{\mathrm{DFT}}, K)$
$k, \mu, \mu_1, \mu_2 \in \{\, 0, 1, \ldots, N_{\mathrm{DFT}} - 1 \,\}$
$H_\rho[\mu_1, \mu_2, \mu_3] = H_\rho[\boldsymbol{\mu}] = H_\rho(\mathrm{e}^{\mathrm{j}\frac{2\pi}{N_{\mathrm{DFT}}}\boldsymbol{\mu}})$
forall λ **do**
  $\boldsymbol{A}_\lambda[\mu] = \mathrm{DFT}\{\, \boldsymbol{a}_\lambda[k] \,\}$
  $\bar{\phi}_\lambda^{\mathrm{SCI}} = -\frac{3}{2}\frac{\phi_{\mathrm{NL},\rho}}{N_{\mathrm{DFT}}^2} \sum_\mu \|\boldsymbol{A}_\lambda[\mu]\|^2$
  $\vec{\boldsymbol{S}}_\lambda^{\mathrm{SCI}} \cdot \vec{\boldsymbol{\sigma}} = -\frac{1}{2}\frac{\phi_{\mathrm{NL},\rho}}{N_{\mathrm{DFT}}^2} \sum_\mu 2\boldsymbol{A}_\lambda[\mu]\boldsymbol{A}_\lambda^{\mathsf{H}}[\mu] - \|\boldsymbol{A}_\lambda[\mu]\|^2 \mathbf{I}$
  forall μ **do**
    $\mu_3 = \mathrm{mod}_{N_{\mathrm{DFT}}}(\mu - \mu_1 + \mu_2)$
    $\mathcal{U} = \{\, [\mu_1, \mu_2]^{\mathsf{T}} \mid \mu_2 \neq \mu_1 \wedge \mu_2 \neq \mu_3 \,\}$
    $\Delta\boldsymbol{A}_\lambda^{\mathrm{SCI}}[\mu] = -\mathrm{j}\frac{\phi_{\mathrm{NL},\rho}}{N_{\mathrm{DFT}}^2}$
      $\times \sum_{\mathcal{U}} \boldsymbol{A}_\lambda[\mu_1]\boldsymbol{A}_\lambda^{\mathsf{H}}[\mu_2]\boldsymbol{A}_\lambda[\mu_3]H_\rho[\mu_1, \mu_2, \mu_3]$
    $\boldsymbol{Y}_\lambda^{\mathrm{PERT}}[\mu] = \exp(\mathrm{j}\bar{\phi}_\lambda^{\mathrm{SCI}}\mathbf{I} + \mathrm{j}\vec{\boldsymbol{S}}_\lambda^{\mathrm{SCI}} \cdot \vec{\boldsymbol{\sigma}})$
      $\times(\boldsymbol{A}_\lambda[\mu] + \Delta\boldsymbol{A}_\lambda^{\mathrm{SCI}}[\mu])$
  end
  $\boldsymbol{y}_\lambda^{\mathrm{PERT}}[k] = \mathrm{DFT}^{-1}\{\, \boldsymbol{Y}_\lambda^{\mathrm{PERT}}[\mu] \,\}$
end
$\langle \boldsymbol{y}^{\mathrm{PERT}}[k] \rangle = \mathrm{overlapSaveAppend}(\boldsymbol{y}_\lambda^{\mathrm{PERT}}[k], N_{\mathrm{DFT}}, K)$

$\boldsymbol{\mu} \in \mathcal{U}_\phi^{\mathrm{SCI}}$, and with that the kernel energy is simplified to $E_{H,\phi}^{\mathrm{SCI}} = (2N_{\mathrm{DFT}} - 1)/N_{\mathrm{DFT}}^2 \approx 2/N_{\mathrm{DFT}}$.

The cross-channel sets are defined according to (76) with only a single degeneracy.

IV. Numerical Results

This section complements the theoretical considerations of the previous sections by numerical simulations. To this end, we compare the simulated received symbol sequence $\langle\, \boldsymbol{y}[k] \,\rangle$ obtained by the perturbation-based (PERT) end-to-end channel models to the sequence obtained by numerical evaluation via the SSFM (in the following indicated by the superscript SSFM).

The evaluated metric is the *normalized* MSE between the two output sequences for a given input sequence $\langle\, \boldsymbol{a}[k] \,\rangle$, i.e., we have

$$\sigma_{\mathrm{e}}^2 \stackrel{\mathrm{def}}{=} \mathrm{E}\{\, \|\boldsymbol{y}^{\mathrm{SSFM}} - \boldsymbol{y}^{\mathrm{PERT}}\|^2 \,\}, \tag{92}$$

where the expectation takes the form of a statistical average of the received sequence over the discrete time index k. The MSE is already normalized due to the fixed variance $\sigma_a^2 = 1$ of the symbol alphabet and the receiver-side re-normalization in (25), s.t. the received sequence has (approximately[20]) the same fixed variance as the transmit sequence.

The simulation parameters are summarized in Table I. A total number of $N_{\mathrm{SYM}} = 2^{16}$ transmit symbols $\langle\, \boldsymbol{a}[k] \,\rangle$ are randomly drawn from a polarization-division multiplex (PDM) 64-ary quadrature amplitude modulation (QAM) symbol alphabet $\mathcal{A}$ with (4D) cardinality $M = |\mathcal{A}| = 4096$, i.e., 64-QAM per polarization. The transmit pulse shape $h_{\mathrm{T}}(t)$ is a RRC with roll-off factor ρ and energy E_{T} to vary the optical launch power[21] P.

TABLE I
Simulation Parameters

$\boldsymbol{a}, \boldsymbol{b} \in \mathcal{A}$	PDM 64-QAM	
M	4096 ($\triangleq$ 64-QAM per polarization)	
$h_{\mathrm{T}}(t)$	$h_{\mathrm{RRC}}(t)$ with roll-off factor ρ	
γ	$1.1\,\mathrm{W}^{-1}\mathrm{km}^{-1}$	
β_2	$-21\,\mathrm{ps}^2/\mathrm{km}$	
$\mathcal{B}_0$	$0\,\mathrm{ps}^2$	
$\mathcal{B}(z)$	$\beta_2 z$	
$10\log_{10}\mathrm{e}^\alpha$	0 dB/km	0.2 dB/km
L_{sp}	21.71 km	100 km
$\mathcal{G}(z)$	0	$-\alpha z + \alpha L_{\mathrm{sp}} \sum_{i=1}^{N_{\mathrm{sp}}} \delta(z - iL_{\mathrm{sp}})$
N_{SYM}	2^{16}	
N_{DFT}	$\max(\, 2^{\lceil \log_2 8_{T,\nu} \rceil + 2},\, 64 \,)$	
$10\log_{10}\Gamma$	$-60\,\mathrm{dB}$	

Two different optical amplification schemes are considered: ideal distributed Raman amplification (i.e., lossless transmission) and *transparent* end-of-span lumped amplification (i.e., lumped amplification where the effect of *signal-gain depletion* [5, Sec. II B.] is neglected in the derivation of the perturbation model). For lumped amplification we consider homogeneous spans of SSMF with fiber attenuation $10\log_{10}\mathrm{e}^\alpha = 0.2$ dB/km and a span length of $L_{\mathrm{sp}} = 100$ km. In case of lossless transmission we have $10\log_{10}\mathrm{e}^\alpha = 0$ dB/km and span length $L_{\mathrm{sp}} = 21.71$ km corresponding to the asymptotic effective length $L_{\mathrm{eff,a}} \stackrel{\mathrm{def}}{=} 1/\alpha$ of a fictitious fiber with infinite length and attenuation $10\log_{10}\mathrm{e}^\alpha = 0.2$ dB/km. The dispersion profile $\mathcal{B}(z) = \beta_2 z$ conforms with modern dispersion uncompensated (DU) links, i.e., without optical inline dispersion compensation and bulk compensation at the receiver-side (typically performed in the digital domain). Dispersion pre-compensation at the transmit-side can be easily incorporated via $\mathcal{B}_0$ but is not considered in this work. The dispersion coefficient is $\beta_2 = -21$ ps^2/km and the nonlinearity coefficient is $\gamma = 1.1$ W^{-1}km^{-1}, both constant over z and ω. Additive noise due to amplified spontaneous emission (ASE) and laser PN are neglected since we only focus on deterministic signal-signal NLI.

The numerical reference simulation is a full-vectorial field simulation implemented via the *symmetric split-step Fourier method* [46] with adaptive step size and a maximum nonlinear phase-rotation per step of $\phi_{\mathrm{NL}}^{\max} = 3.5 \times 10^{-4}$ rad. The simulation bandwidth is $B_{\mathrm{SIM}} = 8R_{\mathrm{s}}$ for single-channel and $16R_{\mathrm{s}}$ for dual-channel transmission. All filter operations (i.e., pulse-shaping, linear step in the SSFM, linear channel matched filter) are performed at the full simulation bandwidth via fast convolution and regarding periodic boundary conditions.

[20] In the numerical simulation via SSFM *signal depletion* takes place due to an energy transfer from signal to NLI. For simplicity, this additional signal energy loss is not accounted for by additional receiver-side re-normalization.

[21] In the previous sections, signals are always treated as dimensionless entities, but by convention we will still associate the optical launch power P with units of [W] and the nonlinearity coefficient γ with [1/(W$\cdot$m)].

A. Discussion of the Results

In Fig. 6 (a), we start our evaluation with the most simple scenario, i.e., single-channel, single-span, and lossless fiber. The MSE is shown in logarithmic scale $10\log_{10}\sigma_{\mathrm{e}}^2$ in dB over the symbol rate R_{s} and the launch power of the probe $10\log_{10}(P_{\rho}/\mathrm{mW})$ in dBm. The results are obtained from the regular (REG) perturbation-based (PERT) end-to-end channel model in discrete time-domain (TD), corresponding to (38). For the given effective length L_{eff} and dispersion parameter β_2, the range of the symbol rate between 1 GBd and 100 GBd corresponds to a map strength $\mathcal{S}_{T,\rho}$ between 0.003 and 28.7. This amounts to virtually no memory of the intra-channel nonlinear interaction for small symbol rates (hence only very few coefficients $h_{\rho}[\boldsymbol{\kappa}]$ exceeding the minimum energy level of $10\log_{10}\Gamma^{\mathrm{SCI}} = -60\,\mathrm{dB}$) to a very broad intra-channel nonlinear memory for high symbol rates (with coefficients $h_{\rho}[\boldsymbol{\kappa}]$ covering a large number of symbols). Likewise, the launch power of the probe P_{ρ} spans a nonlinear phase shift $\phi_{\mathrm{NL},\rho}$ from 0.02 to 0.34 rad. We can observe a gradual increase in σ_{e}^2 of about 5 dB per 1.5 dBm launch power in the nonlinear transmission regime. We deliberately consider a MSE $10\log_{10}\sigma_{\mathrm{e}}^2 > -30\,\mathrm{dB}$ as a *poor* match between the perturbation-based model and the full-field simulation, i.e., here for P_{ρ} larger than 9 dBm ($\triangleq 0.168\,\mathrm{rad} \approx 10°$) independent of R_{s}.

In Fig. 6 (b) the same system scenario is considered but instead of the regular model, now, the regular-logarithmic (REGLOG) model is employed according to (55). The gradual increase in σ_{e}^2 with increasing P_{ρ} is now considerably relaxed to about 5 dB per 2.5 dBm launch power. The region of poor model match with $10\log_{10}\sigma_{\mathrm{e}}^2 > -30\,\mathrm{dB}$ is now only approached for launch powers larger than 12 dBm. We can also observe that σ_{e}^2 improves with increasing symbol rate R_{s}, in particular for rates $R_{\mathrm{s}} > 40$ GBd. This is explained by the fact that the kernel energy E_h^{SCI} in (73) depends on the symbol rate R_{s} s.t. σ_{e}^2 is reduced for higher symbol rates.

Fig. 7 (a) shows the energy of the (time-domain) kernel coefficients E_h^{SCI} over R_{s} for a single-span SSMF with $L_{\mathrm{sp}} = 100\,\mathrm{km}$ and for a lossless fiber with $L_{\mathrm{sp}} = 21.71\,\mathrm{km}$. Generally, we see that E_h^{SCI} is constant for small R_{s} and then curves into a transition region towards smaller energies for increasing R_{s}. For transmission over SSMF this transition region is shifted to smaller R_{s}, e.g., E_h^{SCI} drops from 0.7 to 0.6 around 33 GBd for lossless transmission and at around 20 GBd for transmission over SSMF. We also present the kernel energies $E_{h,\Delta}^{\mathrm{SCI}}$ associated with additive perturbations, and $E_{h,\phi}^{\mathrm{SCI}}$ associated with multiplicative perturbations. For this single-span scenario, most of the energy is concentrated in $E_{h,\phi}^{\mathrm{SCI}}$, i.e., corresponding to the degenerate symbol combinations with $\kappa_1 = 0$ or $\kappa_3 = 0$ defined in (58)–(60). Interestingly, while the total energy E_h^{SCI} decreases monotonically with R_{s}, the additive contribution $E_{h,\Delta}^{\mathrm{SCI}}$ increases in the transition region and then decreases again for large R_{s}. This behaviour is also visible in the results presented in Fig. 6 (a) and (b).

Fig. 7 (b) shows the energy of the kernel coefficients E_H^{SCI} in frequency-domain for the same system scenario as in (a). The total energies are the same, i.e., $E_h^{\mathrm{SCI}} = E_H^{\mathrm{SCI}}$ (cf. Parseval's theorem), however, the majority of the energy is now contained in the regular (additive) subset of coefficients. The energy of the degenerate, i.e., multiplicative, subset of coefficients $E_{H,\phi}^{\mathrm{SCI}}$ depends on the frequency discretization (which coincides here with the transformation length N_{DFT}) and is approximately $2/N_{\mathrm{DFT}}$. The exact value $(2N_{\mathrm{DFT}} - 1)/N_{\mathrm{DFT}}^2$ would be achieved for $\rho = 0$. For $R_{\mathrm{s}} > 75.1$ GBd we have $\mathcal{S}_{T,\rho} > 16$ and it can be seen that $E_{H,\phi}^{\mathrm{SCI}}$ drops from $1/32$ to $1/64$ and $E_{H,\Delta}^{\mathrm{SCI}}$ jumps up by an equal amount because N_{DFT} increases from 64 to 128 (cf. the set of simulation parameters in Table I). The REGLOG frequency-domain model is hence pre-dominantly a regular model, where only the average multiplicative effects are truly treated as such.

In Fig. 8 (a) and (b) the respective results on σ_{e}^2 using the discrete frequency-domain (FD) model according to Algorithm 1 and 2 are shown. We can confirm our previous statement that the regular perturbation model in time and frequency are equivalent considering that the results shown in Fig. 6 (a) and Fig. 8 (a) are (virtually) the same. We also conclude that the REGLOG-FD performs very similar to the corresponding TD model despite the fact that only *average* terms are considered

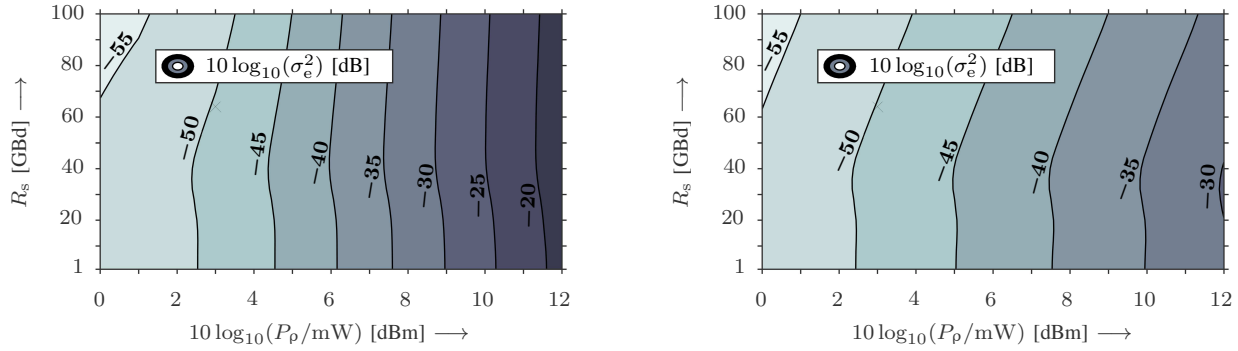

(a) REG-PERT-TD, single-channel, single-span, lossless fiber

(b) REGLOG-PERT-TD, single-channel, single-span, lossless fiber

Fig. 6. Contour plot of the normalized mean-square error $\sigma_{\mathrm{e}}^2 = \mathrm{E}\{\|\boldsymbol{y}^{\mathrm{SSFM}} - \boldsymbol{y}^{\mathrm{PERT}}\|^2\}$ in dB between the perturbation-based (PERT) end-to-end model and the split-step Fourier method (SSFM). The results are shown w.r.t. the symbol rate R_{s} and the optical launch power of the probe P_{ρ} in dBm. Parameters as in Table I with roll-off factor $\rho = 0.2$, $N_{\mathrm{sp}} = 1$, $10\log_{10}\mathrm{e}^{\alpha} = 0\,\mathrm{dB/km}$ and $L_{\mathrm{sp}} = 21.71\,\mathrm{km}$. In (a) the regular (REG) time-domain (TD) model is carried out as in (38) and in (b) the regular-logarithmic (REGLOG) model is carried out as in (55).

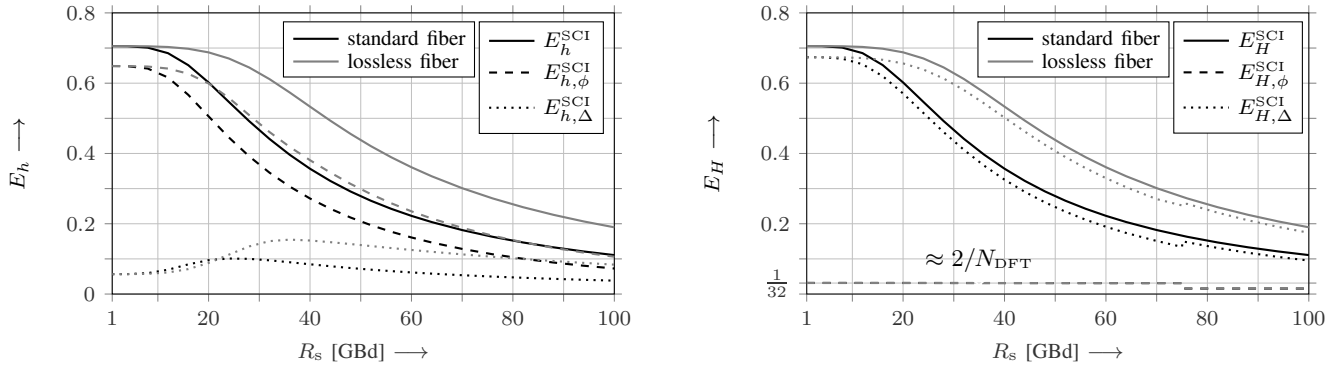

(a) PERT-TD, single-channel, single-span

(b) PERT-FD, single-channel, single-span

Fig. 7. Energy of the kernel coefficients in time-domain E_h (a) and in frequency-domain E_H (b) over the symbol rate R_s. The kernel coefficients are obtained from the regular-logarithmic (REGLOG) model for a single-channel ($\rho = 0.2$) over a standard single-mode fiber ($10\log_{10}\mathrm{e}^{\alpha} = 0.2\,\mathrm{dB/km}$ and $L_{\mathrm{sp}} = 100\,\mathrm{km}$) or a lossless fiber ($10\log_{10}\mathrm{e}^{\alpha} = 0\,\mathrm{dB/km}$ and $L_{\mathrm{sp}} = 21.71\,\mathrm{km}$). The subscript Δ denotes the subset of all coefficients associated with additive perturbations and the subscript ϕ denotes the subset of all coefficients with multiplicative perturbations.

as multiplicative distortions. This may motivate the application of the FD over the TD model for fiber nonlinearity mitigation when an implementation in frequency-domain is computationally more efficient.

Fig. 9 (a) shows σ_e^2 for a single-channel over standard single-mode fiber ($L_{\mathrm{sp}} = 100\,\mathrm{km}$ and $10\log_{10}\mathrm{e}^{\alpha} = 0.2\,\mathrm{dB/km}$) and lumped end-of-span amplification. In the full-field simulation, the lumped amplifier is operated in *constant-gain* mode compensating for the exact span-loss of 20 dB. The results over a single-span in Fig. 9 (a) are very similar in the low symbol rate regime compared to the lossless case in Fig. 6 (b). For R_s larger than 20 GBd, the MSE starts to decrease at a higher rate compared to the lossless case. This is in line with the energy of the kernel coefficients E_h^{SCI} for the standard fiber shown in Fig. 7 (a).

In Fig. 9 (b), σ_e^2 is shown over the roll-off factor ρ and the number of spans N_{sp} for a fixed symbol rate of $R_\mathrm{s} = 64\,\mathrm{GBd}$ and a fixed launch power of $10\log_{10}(P_\rho/\mathrm{mW}) = 3\,\mathrm{dBm}$. The black cross in Fig. 9 (a) and (b) indicates the point with a common set of parameters. We can see a dependency on the roll-off factor ρ which is due to a dependency of E_h^{SCI} on ρ (not shown here). With increasing ρ the kernel energy E_h^{SCI} decreases and hence does σ_e^2 too.

The scaling laws of σ_e^2 with N_{sp} are complemented in Fig. 10 (a) by the energy of the kernel coefficients E_h^{SCI} for the same system scenario as in Fig. 9 (b) (with $\rho = 0.2$). It is interesting to see that (for this particular system scenario) $E_{h,\Delta}^{\mathrm{SCI}}$ and $E_{h,\phi}^{\mathrm{SCI}}$ intersect at $N_{\mathrm{sp}} = 2$. We can conclude that after the second span more energy is comprised within the additive subset of coefficients than in the multiplicative one. With increasing N_{sp} the relative contribution of $E_{h,\Delta}^{\mathrm{SCI}}$ to the total energy E_h^{SCI} is increasing. Note, while E_h^{SCI} is actually monotonically decreasing with N_{sp}, the common prefactor $\phi_{\mathrm{NL},\rho}$ has to be factored in as it effectively scales the nonlinear distortion. Since for heterogeneous spans we have $\phi_{\mathrm{NL},\rho} \propto L_{\mathrm{eff}} \propto N_{\mathrm{sp}}$, the same traces are shown scaled by N_{sp}^2 to illustrate how the energy of the total distortion accumulates with increasing transmission length. In this respect, similar results can be obtained from the presented channel model as from the GN-model (given proper scaling with $\phi_{\mathrm{NL},\rho}^2$ instead of just N_{sp}^2, and similarly taking all other wavelength channels into account). Additionally, qualitative statements

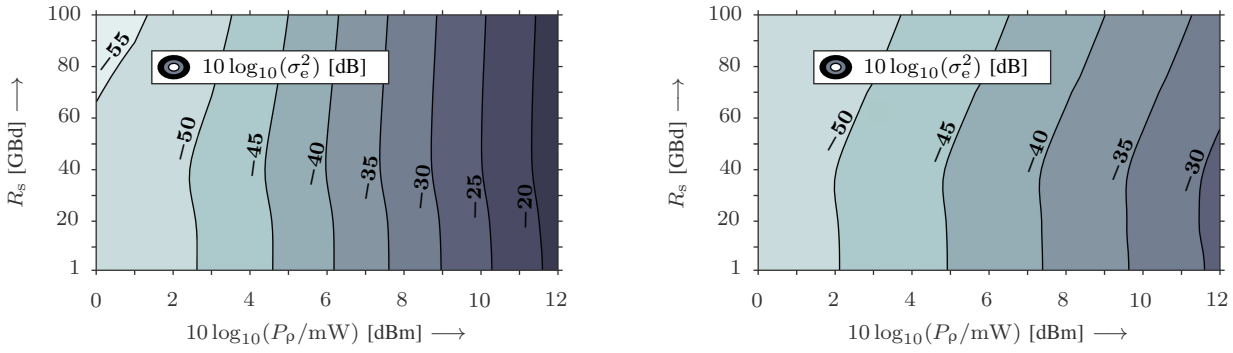

(a) REG-PERT-FD, single-channel, single-span, lossless fiber

(b) REGLOG-PERT-FD, single-channel, single-span, lossless fiber

Fig. 8. Contour plot of the normalized mean-square error σ_e^2 in dB. The results are shown w.r.t. the symbol rate R_s and the optical launch power of the probe P_ρ in dBm. Parameters as in Table I with roll-off factor $\rho = 0.2$, $N_{\mathrm{sp}} = 1$, $10\log_{10}\mathrm{e}^{\alpha} = 0\,\mathrm{dB/km}$ and $L_{\mathrm{sp}} = 21.71\,\mathrm{km}$. In (a) the regular (REG) frequency-domain (FD) model is carried out as in Algorithm 1 and in (b) the regular-logarithmic (REGLOG) model is carried out as in Algorithm 2.

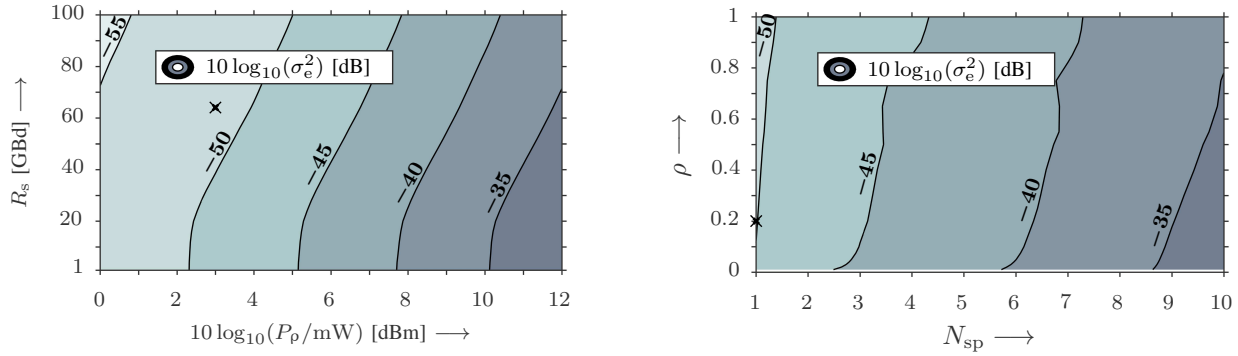

(a) REGLOG-PERT-TD, single-channel, single-span, standard fiber

(b) REGLOG-PERT-TD, single-channel, multi-span, standard fiber

Fig. 9. Contour plot of the normalized mean-square error σ_e^2 in dB. The results are obtained from the regular-logarithmic (REGLOG) time-domain (TD) model over a standard single-mode fiber ($10\log_{10}\mathrm{e}^{\alpha} = 0.2\,\mathrm{dB/km}$ and $L_\mathrm{sp} = 100\,\mathrm{km}$) with end-of-span lumped amplification. In (a) the symbol rate R_s and the optical launch power P_ρ are varied for single-span ($N_\mathrm{sp} = 1$) transmission and fixed roll-off factor ($\rho = 0.2$). In (b) the roll-off factor ρ and number of spans N_sp are varied with fixed symbol rate ($R_\mathrm{s} = 64\,\mathrm{GBd}$) and fixed launch power ($10\log_{10}(P_\rho/\mathrm{mW}) = 3\,\mathrm{dBm}$). The black marker indicates the joint reference point.

can be derived, e.g., whether the nonlinear distortion is predominantly additive or multiplicative or on which time scale nonlinear distortions are still correlated.

Fig. 11 shows the σ_e^2 for dual-channel transmission using either the REGLOG time-domain (a) or frequency-domain model (b). The transmit symbols of the interferer $\langle \boldsymbol{b}[k] \rangle$ are drawn from the same symbol set $\mathcal{A}$, i.e., 64-QAM per polarization. For both wavelength channels, the symbol rate is fixed to $R_\mathrm{s} = 64\,\mathrm{GBd}$ and the roll-off factor of the RRC shape is $\rho = 0.2$. The transmit power of the probe is set to $10\log_{10}(P_\rho/\mathrm{mW}) = 0\,\mathrm{dBm}$ while the transmit power of the interferer P_ν with channel number $\nu = 1$ is varied together with the relative frequency offset $\Delta\omega_1/(2\pi)$ ranging from 76.8 GHz (i.e., no guard interval with $(1+\rho)\times 64\,\mathrm{GHz}$) to 200 GHz. In the numerical simulation via SSFM we use an ideal channel combiner and both wavelength channels co-propagate at the full simulation bandwidth $B_\mathrm{SIM} = 16R_\mathrm{s}$. In case of the end-to-end channel model both contributions from intra- and inter-channel distortions are combined into a single perturbative term (cf. (55) and (78)). The baseline error σ_e^2 is therefore approximately $-55\,\mathrm{dB}$ considering the respective case with $R_\mathrm{s} = 64\,\mathrm{GBd}$ and $P_\rho = 0\,\mathrm{dBm}$ in Fig. 6 (b). It is seen that the time- and frequency-domain model perform very similar. The dependency on the channel spacing $\Delta\omega_1$ is explained considering Fig. 10 (b). Here, the energy of the cross-channel coefficients $h_1[\boldsymbol{\kappa}]$ is shown over $\Delta\omega_1$. Generally, with increasing $\Delta\omega_1$, E_h^XCI decreases and additionally the relative contribution of the degeneracy at $\kappa_3 = 0$, i.e., $E_{h,\phi}^\mathrm{SCI}$, is growing. Ultimately, the main distortion caused by an interferer spaced far away from the probe channel is a distortion in phase and state of polarization.

V. Summary and Conclusion

In this paper, a comprehensive analysis of end-to-end channel models for fiber-optic transmission based on a perturbation approach is presented. The existing view on nonlinear interference following the *pulse collision picture* is described

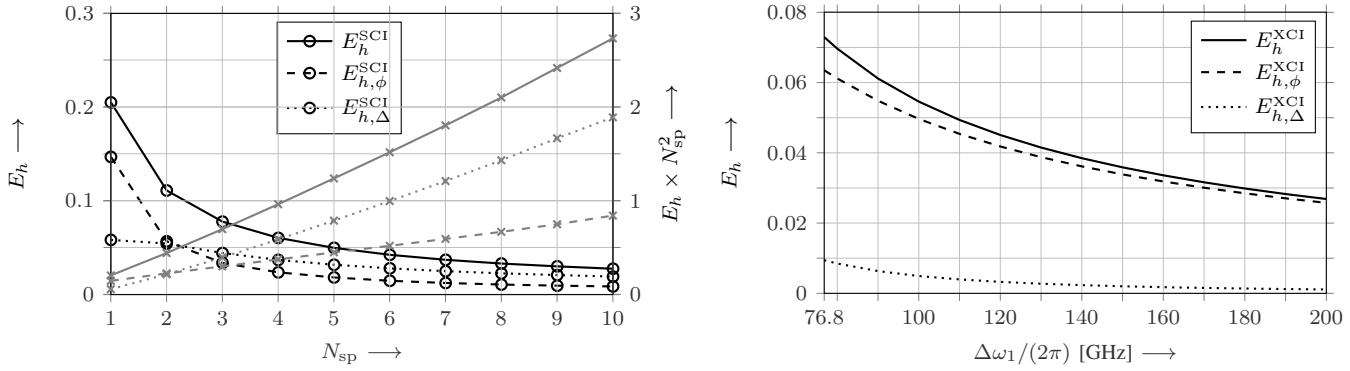

(a) PERT-TD, single-channel, multi-span, standard fiber

(b) PERT-TD, dual-channel, single-span, lossless fiber

Fig. 10. In (a), the energy of the kernel coefficients (black lines, bullet markers, left y-axis) in time-domain E_h is shown over N_sp spans of standard single-mode fiber ($10\log_{10}\mathrm{e}^{\alpha} = 0.2\,\mathrm{dB/km}$ and $L_\mathrm{sp} = 100\,\mathrm{km}$, $\rho = 0.2$). Additionally, the kernel energies are shown scaled with $N_\mathrm{sp}^2 \propto \phi_{\mathrm{NL},\rho}^2$ (gray lines, cross markers, right y-axis) to indicate the general growth of nonlinear distortions with increasing N_sp (similar to the GN-model). In (b), kernel energies E_h are shown for cross-channel interference (XCI) imposed by a single wavelength channel spaced at $\Delta\omega_1/(2\pi)\,\mathrm{GHz}$ over a single span of lossless fiber. Both probe and interferer have $R_\mathrm{s} = 64\,\mathrm{GBd}$ and $\rho = 0.2$.

in a unified framework with a novel frequency-domain perspective that incorporates the time-discretization via an aliased frequency-domain kernel. The relation between the time- and frequency-domain representation is elucidated and we show that the kernel coefficients in both views are related by a 3D discrete-time Fourier transform. The energy of the kernel coefficients can be directly related to the GN-model.

While the pulse collision picture is a theory developed particularly for *inter*-channel nonlinear interactions, a generalization to *intra*-channel nonlinear interactions is presented. An intra-channel phase distortion term and an intra-channel XPolM term are introduced and both correspond to a subset of degenerate intra-channel pulse collisions. In analogy to the time-domain model, the frequency-domain model is modified to treat certain degenerate mixing products as multiplicative distortions. As a result, we have established a complete formulation of strictly *regular* (i.e., additive) models, and *regular-logarithmic* (i.e., mixed additive and multiplicative) models—both in time- and in frequency-domain, both for intra- and inter-channel nonlinear interference.

Derived from the frequency-domain description, a novel class of algorithms is proposed which effectively computes the end-to-end relation between transmit and receive sequences over discrete frequencies from the Nyquist interval. In fiber nonlinearity compensation this scheme can be well applied at the transmit-side before pulse-shaping or on the receive-side after matched filtering. Moreover, while the time-domain implementation requires a triple summation per time-instance, the frequency-domain implementation involves only a double summation per frequency index. Similar as for linear systems, this characteristic allows for very efficient implementations using the fast Fourier transform when the time-domain kernel comprises many coefficients.

The derived algorithms were compared to the (oversampled and inherently sequential) split-step Fourier method based on the mean-squared error between both output sequences. We show that, in particular, the regular-logarithmic models have good agreement with the split-step Fourier method over a wide range of system parameters but have significantly lower numerical complexity. The presented results are further supported by a qualitative analysis involving the kernel energies to quantify the relative contributions of either additive or multiplicative distortions.

Appendix A
Proof of the relation in (32), (33)

In this appendix we compute the Fourier transform of $\Delta\boldsymbol{s}(t)$ in (33) similar to [30, Appx.].

We start our derivation by expressing the optical field envelope $\boldsymbol{u}(0,t)$ by its inverse Fourier transform of $\boldsymbol{U}(0,\omega)$ to obtain

$$\begin{aligned}\Delta\boldsymbol{s}(t) =& -\mathrm{j}\gamma\frac{8}{9}L_{\mathrm{eff}}\int_{\mathbb{R}^2} h_{\mathrm{NL}}(\tau_1,\tau_2) \\ &\times \boldsymbol{u}(0,t+\tau_1)\boldsymbol{u}^{\mathsf{H}}(0,t+\tau_1+\tau_2)\boldsymbol{u}(t+\tau_2)\mathrm{d}^2\boldsymbol{\tau} \\ =& -\mathrm{j}\gamma\frac{8}{9}L_{\mathrm{eff}}\frac{1}{(2\pi)^3}\iint_{-\infty}^{+\infty}\mathrm{d}\tau_1\mathrm{d}\tau_2\; h_{\mathrm{NL}}(\tau_1,\tau_2) \\ &\times\int_{-\infty}^{\infty}\mathrm{d}\omega_3\boldsymbol{U}(0,\omega_3)\exp(\mathrm{j}\omega_3\tau_1) \\ &\times\int_{-\infty}^{\infty}\mathrm{d}\omega_2\boldsymbol{U}^{\mathsf{H}}(0,\omega_2)\exp(-\mathrm{j}\omega_2(\tau_1+\tau_2)) \\ &\times\int_{-\infty}^{\infty}\mathrm{d}\omega_1\boldsymbol{U}(0,\omega_1)\exp(\mathrm{j}\omega_1\tau_2) \\ &\times\exp(\mathrm{j}(\omega_3-\omega_2+\omega_1)t).\end{aligned} \tag{93}$$

The Fourier transform of the former expression yields

$$\begin{aligned}\Delta\boldsymbol{S}(\omega) =& -\mathrm{j}\gamma\frac{8}{9}L_{\mathrm{eff}}\frac{1}{(2\pi)^3}\iiint_{-\infty}^{+\infty}\mathrm{d}t\mathrm{d}\tau_1\mathrm{d}\tau_2\; h_{\mathrm{NL}}(\tau_1,\tau_2) \\ &\times\int_{-\infty}^{\infty}\mathrm{d}\omega_3\boldsymbol{U}(0,\omega_3)\exp(\mathrm{j}\omega_3\tau_1) \\ &\times\int_{-\infty}^{\infty}\mathrm{d}\omega_2\boldsymbol{U}^{\mathsf{H}}(0,\omega_2)\exp(-\mathrm{j}\omega_2(\tau_1+\tau_2)) \\ &\times\int_{-\infty}^{\infty}\mathrm{d}\omega_1\boldsymbol{U}(0,\omega_1)\exp(\mathrm{j}\omega_1\tau_2) \\ &\times\exp(\mathrm{j}(\omega_3-\omega_2+\omega_1-\omega)t).\end{aligned} \tag{94}$$

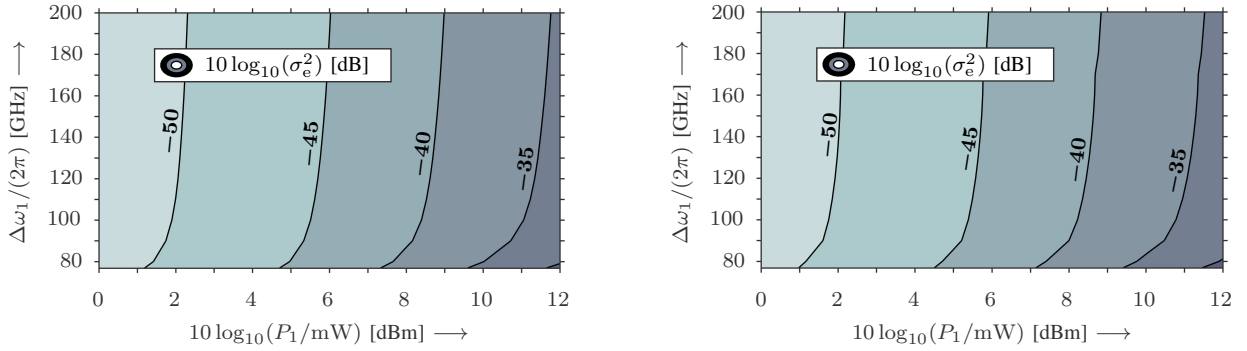

(a) REGLOG-PERT-TD, dual-channel, single-span, lossless fiber

(b) REGLOG-PERT-FD, dual-channel, single-span, lossless fiber

Fig. 11. Contour plot of the normalized mean-square error σ_{e}^2 in dB. The results are obtained from two co-propagating wavelength channels with PDM 64-QAM and a symbol rate of 64 GBd and roll-off factor $\rho = 0.2$. The launch power of the probe is fixed at $10\log_{10}(P_\rho/\mathrm{mW}) = 0\,\mathrm{dBm}$ while the power of the interferer P_1 and the relative frequency offset $\Delta\omega_1$ are varied. In (a) the regular-logarithmic (REGLOG) time-domain (TD) model for both SCI and XCI is carried out as in (55) and in (b) the REGLOG frequency-domain (FD) model is carried out as in Algorithm 2 and (78) for both SCI and XCI.

We now use the identity $\int_{-\infty}^{\infty}\exp(\mathrm{j}(\omega_3-\omega_2+\omega_1-\omega)t)\mathrm{d}t = 2\pi\delta(\omega_3-\omega_2+\omega_1-\omega)$ to obtain

$$\begin{aligned}\Delta\boldsymbol{S}(\omega) = &-\mathrm{j}\gamma\frac{8}{9}L_{\mathrm{eff}}\frac{1}{(2\pi)^2}\iint_{-\infty}^{+\infty}\mathrm{d}\tau_1\mathrm{d}\tau_2\; h_{\mathrm{NL}}(\tau_1,\tau_2)\\ &\times\boldsymbol{U}(0,\omega-\omega_1+\omega_2)\exp(\mathrm{j}(\omega-\omega_1+\omega_2)\tau_1)\\ &\times\int_{-\infty}^{\infty}\mathrm{d}\omega_2\boldsymbol{U}^{\mathsf{H}}(0,\omega_2)\exp(-\mathrm{j}\omega_2(\tau_1+\tau_2))\\ &\times\int_{-\infty}^{\infty}\mathrm{d}\omega_1\boldsymbol{U}(0,\omega_1)\exp(\mathrm{j}\omega_1\tau_2).\end{aligned}\tag{95}$$

After re-arranging the order of integration, we have

$$\begin{aligned}\Delta\boldsymbol{S}(\omega) = &-\mathrm{j}\gamma\frac{8}{9}L_{\mathrm{eff}}\frac{1}{(2\pi)^2}\iint_{-\infty}^{+\infty}\mathrm{d}\omega_1\mathrm{d}\omega_2\\ &\times\boldsymbol{U}(0,\omega-\omega_1+\omega_2)\boldsymbol{U}^{\mathsf{H}}(0,\omega_2)\boldsymbol{U}(0,\omega_1)\\ &\times\iint_{-\infty}^{\infty}\mathrm{d}\tau_1\mathrm{d}\tau_2 h_{\mathrm{NL}}(\tau_1,\tau_2)\exp(\mathrm{j}\omega_1\tau_2)\\ &\times\exp(-\mathrm{j}\omega_2(\tau_1+\tau_2))\exp(\mathrm{j}(\omega-\omega_1+\omega_2)\tau_1).\end{aligned}\tag{96}$$

And finally a change of variables with $\upsilon_1=\omega_1-\omega$ and $\upsilon_2=\omega_2-\omega_1$ yields

$$\begin{aligned}\Delta\boldsymbol{S}(\omega) = &-\mathrm{j}\gamma\frac{8}{9}L_{\mathrm{eff}}\frac{1}{(2\pi)^2}\iint_{-\infty}^{+\infty}\mathrm{d}\upsilon_1\mathrm{d}\upsilon_2\\ &\times\boldsymbol{U}(0,\omega+\upsilon_2)\boldsymbol{U}^{\mathsf{H}}(0,\omega+\upsilon_1+\upsilon_2)\boldsymbol{U}(0,\omega+\upsilon_1)\\ &\times\underbrace{\iint_{-\infty}^{\infty}\mathrm{d}\tau_1\mathrm{d}\tau_2 h_{\mathrm{NL}}(\tau_1,\tau_2)\exp(-\mathrm{j}\upsilon_1\tau_1-\mathrm{j}\upsilon_2\tau_2)}_{H_{\mathrm{NL}}(\upsilon_1,\upsilon_2)=\mathcal{F}\{\,h_{\mathrm{NL}}(\tau_1,\tau_2)\,\}},\end{aligned}\tag{97}$$

which is equivalent to the expression in (32). □

REFERENCES

[1] S. J. Savory, "Digital Coherent Optical Receivers: Algorithms and Subsystems," *IEEE J. Sel. Top. Quantum Electron.*, vol. 16, no. 5, pp. 1164–1179, 2010.

[2] D. Zwillinger, *Handbook of Differential Equations (eprint)*. Academic Press, 3rd ed., 1998.

[3] K. V. Peddanarappagari and M. Brandt-Pearce, "Volterra Series Transfer Function of Single-mode Fibers," *J. Lightwave Technol.*, vol. 15, no. 12, pp. 2232–2241, 1997.

[4] A. Vannucci, P. Serena, and A. Bononi, "The RP Method: A New Tool for The Iterative Solution of the Nonlinear Schrödinger Equation," *J. Lightwave Technol.*, vol. 20, no. 7, pp. 1102–1112, 2002.

[5] A. Ghazisaeidi, "A Theory of Nonlinear Interactions Between Signal and Amplified Spontaneous Emission Noise in Coherent Wavelength Division Multiplexed Systems," *J. Lightwave Technol.*, vol. 35, no. 23, pp. 5150–5175, 2017.

[6] A. Mecozzi, C. B. Clausen, and M. Shtaif, "Analysis of Intrachannel Nonlinear Effects in Highly Dispersed Optical Pulse Transmission," *IEEE Photonics Technol. Lett.*, vol. 12, no. 4, pp. 392–394, 2000.

[7] A. Mecozzi, C. B. Clausen, and M. Shtaif, "System Impact of Intrachannel Nonlinear Effects in Highly Dispersed Optical Pulse Transmission," *IEEE Photonics Technol. Lett.*, vol. 12, no. 12, pp. 1633–1635, 2000.

[8] A. Mecozzi, C. B. Clausen, M. Shtaif, S. G. Park, and A. H. Gnauck, "Cancellation of Timing and Amplitude Jitter in Symmetric Links Using Highly Dispersed Pulses," *IEEE Photonics Technol. Lett.*, vol. 13, no. 5, pp. 445–447, 2001.

[9] A. Mecozzi, "A Unified Theory of Intrachannel Nonlinearity in Pseudolinear Transmission," in *Impact of Nonlinearities on Fiber Optic Communications*, pp. 253–291, Springer Science & Business Media, 2011.

[10] A. Mecozzi and R. Essiambre, "Nonlinear Shannon Limit in Pseudolinear Coherent Systems," *J. Lightwave Technol.*, vol. 30, no. 12, pp. 2011–2024, 2012.

[11] R. Dar, M. Feder, A. Mecozzi, and M. Shtaif, "Properties of Nonlinear Noise in Long, Dispersion-Uncompensated Fiber Links," *Opt. Express*, vol. 21, no. 22, pp. 25685–25699, 2013.

[12] R. Dar, M. Feder, A. Mecozzi, and M. Shtaif, "Accumulation of Nonlinear Interference Noise in Fiber-Optic Systems," *Opt. Express*, vol. 22, no. 12, pp. 14199–14211, 2014.

[13] R. Dar, M. Feder, A. Mecozzi, and M. Shtaif, "Pulse Collision Picture of Inter-Channel Nonlinear Interference in Fiber-Optic Communications," *J. Lightwave Technol.*, vol. 34, no. 2, pp. 593–607, 2016.

[14] A. V. Oppenheim and A. S. Willsky, *Signals and Systems*. Prentice Hall, 1983.

[15] G. P. Agrawal, *Fiber-Optic Communication Systems*. John Wiley & Sons, Inc., 4th ed., 2010.

[16] I. Kaminow, *Optical Fiber Telecommunications Volume VIB, Systems and Networks*. Elsevier Science Publishing, 6th ed., 2013.

[17] R. Engelbrecht, *Nichtlineare Faseroptik: Grundlagen und Anwendungsbeispiele*. Springer-Verlag, 2015.

[18] R. F. H. Fischer, *Precoding and Signal Shaping for Digital Transmission*. John Wiley & Sons, 2002.

[19] K. D. Kammeyer, *Nachrichtenübertragung*. Vieweg + Teubner, 2008.

[20] J. P. Gordon and H. Kogelnik, "PMD Fundamentals: Polarization Mode Dispersion in Optical Fibers," *Proc. Natl. Acad. Sci. U.S.A.*, vol. 97, no. 9, pp. 4541–50, 2000.

[21] P. Johannisson and M. Karlsson, "Perturbation Analysis of Nonlinear Propagation in a Strongly Dispersive Optical Communication System," *J. Lightwave Technol.*, vol. 31, no. 8, pp. 1273–1282, 2013.

[22] H. Louchet, A. Hodzic, K. Petermann, A. Robinson, and R. Epworth, "Simple Criterion for the Characterization of Nonlinear Impairments in Dispersion-Managed Optical Transmission Systems," *IEEE Photonics Technol. Lett.*, vol. 17, no. 10, pp. 2089–2091, 2005.

[23] X. Wei, "Power-Weighted Dispersion Distribution Function Long-haul Optical Transmission Links," *Opt. Lett.*, vol. 31, no. 17, pp. 2544–2546, 2006.

[24] L. Liu, L. Li, Y. Huang, K. Cui, Q. Xiong, F. N. Hauske, C. Xie, and Y. Cai, "Intrachannel Nonlinearity Compensation by Inverse Volterra Series Transfer Function," *J. Lightwave Technol.*, vol. 30, no. 3, pp. 310–316, 2012.

[25] R. W. Boyd, *Nonlinear Optics*. Academic Press, 3rd ed., 2008.

[26] P. Poggiolini, G. Bosco, A. Carena, V. Curri, Y. Jiang, and F. Forghieri, "A Detailed Analytical Derivation of the GN Model of Non-Linear Interference in Coherent Optical Transmission Systems," *arXiv Prepr. arXiv1209.0394v13*, no. 1209.0394, pp. 1–24, 2012.

[27] P. Poggiolini, "The GN Model of Non-linear Propagation in Uncompensated Coherent Optical Systems," *J. Lightwave Technol.*, vol. 30, no. 24, pp. 3857–3879, 2012.

[28] A. Bononi, P. Serena, and A. Orlandini, "A Unified Design Framework for Terrestrial Systems," *J. Lightwave Technol.*, vol. 26, no. 22, pp. 3617–3631, 2008.

[29] J. K. Fischer, C.-A. Bunge, and K. Petermann, "Equivalent Single-Span Model for Dispersion-Managed Fiber-Optic Transmission Systems," *J. Lightwave Technol.*, vol. 27, no. 16, pp. 3425–3432, 2009.

[30] M. J. Ablowitz and T. Hirooka, "Managing Nonlinearity in Strongly Dispersion-managed Optical Pulse Transmission," *J. Opt. Soc. Am. B Opt. Phys.*, vol. 19, no. 3, pp. 425–439, 2002.

[31] M. J. Ablowitz and T. Hirooka, "Resonant Nonlinear Intrachannel Interactions in Strongly Dispersion-managed Transmission Systems," *Opt. Lett.*, vol. 25, no. 24, pp. 1750–1752, 2000.

[32] I. R. Gabitov and S. K. Turitsyn, "Averaged Pulse Dynamics in a Cascaded Transmission System with Passive Dispersion Compensation," *Opt. Lett.*, vol. 21, no. 5, pp. 327–329, 1996.

[33] R. Dar, "Analytical and Semi-Analytical Models for Nonlinear Transmission," in *42th Eur. Conf. Opt. Commun.*, no. W.1.D.5, 2016.

[34] A. Carena, V. Curri, G. Bosco, P. Poggiolini, and F. Forghieri, "Modeling of the Impact of Nonlinear Propagation Effects in Uncompensated Optical Coherent Transmission Links," *J. Lightwave Technol.*, vol. 30, no. 10, pp. 1524–1539, 2012.

[35] F. Frey, R. Emmerich, C. Schubert, J. K. Fischer, and R. F. H. Fischer, "Improved Perturbation-based Fiber Nonlinearity Compensation," in *44th Eur. Conf. Opt. Commun.*, no. Tu1F.6, 2018.

[36] J. J. Shynk, "Frequency-Domain and Multirate Adaptive Filtering," *IEEE Signal Process Mag.*, vol. 9, no. 1, pp. 14–37, 1992.

[37] F. P. Guiomar and A. N. Pinto, "Simplified Volterra Series Nonlinear Equalizer for Polarization-multiplexed Coherent Optical Systems," *J. Lightwave Technol.*, vol. 31, no. 23, pp. 3879–3891, 2013.

[38] B. Xu and M. Brandt-Pearce, "Modified Volterra Series Transfer Function Method," *IEEE Photonics Technol. Lett.*, vol. 14, no. 1, pp. 47–49, 2002.

[39] B. Xu and M. Brandt-Pearce, "Modified Volterra Series Transfer Function Method and Applications to Fiber-Optic Communications," in *35th Annu. Asilomar Conf. Signals, Syst. Comput.*, pp. 23–27, 2001.
[40] Y. Fan, L. Dou, Z. Tao, L. Lei, S. Oda, T. Hoshida, and J. C. Rasmussen, "Modulation Format Dependent Phase Noise Caused by Intra-channel Nonlinearity," in *38th Eur. Conf. Opt. Commun.*, no. We.2.C.3, 2012.
[41] Z. Tao, Y. Zhao, Y. Fan, L. Dou, T. Hoshida, and J. Rasmussen, "Analytical Intrachannel Nonlinear Models to Predict the Nonlinear Noise Waveform," *J. Lightwave Technol.*, vol. 33, no. 10, pp. 2111–2119, 2014.
[42] M. Secondini, E. Forestieri, and C. R. Menyuk, "A Combined Regular-Logarithmic Perturbation Method for Signal-Noise Interaction in Amplified Optical Systems," *J. Lightwave Technol.*, vol. 27, no. 16, pp. 3358–3369, 2009.
[43] M. Winter, C.-A. Bunge, D. Setti, and K. Petermann, "A Statistical Treatment of Cross-Polarization Modulation in DWDM Systems," *J. Lightwave Technol.*, vol. 27, no. 17, pp. 3739–3751, 2009.
[44] P. Serena and A. Bononi, "On the Nonlinear Reference Phase in Regular Perturbation Models," in *2015 Tyrrhenian Int. Work. Digit. Commun.*, no. 1–4, 2015.
[45] A. Mecozzi and F. Matera, "Polarization Scattering by Intra-channel Collisions," *Opt. Express*, vol. 20, no. 2, pp. 1213–1218, 2012.
[46] O. V. Sinkin, R. Holzlohner, J. Zweck, and C. R. Menyuk, "Optimization of the Split-step Fourier Method in Modeling Optical-fiber Communications Systems," *J. Lightwave Technol.*, vol. 21, no. 1, pp. 61–68, 2003.

Felix Frey received the Dipl.-Ing. degree in electrical engineering from the Karlsruhe Institute of Technology, Karlsruhe, Germany, in 2012. From 2012 to 2016, he was a member of the Scientific Staff at the Fraunhofer Institute for Telecommunications, Heinrich-Hertz-Institute, Berlin, Germany. He is currently pursuing the Ph.D. degree at the Institute of Communications Engineering, Ulm University, Ulm, Germany. His research interest includes digital signal processing, coded modulation and channel models for optical transmission systems.

Johannes K. Fischer (S'04–M'09–SM'15) received the Dipl.-Ing. and Dr.-Ing. degrees in electrical engineering from Technische Universität Berlin, Berlin, Germany, in 2003 and 2009, respectively. In 2010, he joined the Fraunhofer Institute for Telecommunications, Heinrich Hertz Institute, Berlin, Germany, where he is currently heading a research group on digital signal processing with the Department of Photonic Networks and Systems. He has authored or co-authored over 80 articles and a book chapter. His research interests include advanced modulation formats, digital signal processing for optical systems, and realtime implementation of digital signal processing algorithms. Dr. Fischer is a member of the Verband der Elektrotechnik Elektronik Informationstechnik. In 2005, he received the Best Student Paper Award of the Asia-Pacific Optical Communications Conference.

Robert F.H. Fischer (S'93–A'96–M'99–SM'10) received the Dr.-Ing. and Habilitation degrees from the University of Erlangen-Nürnberg, Erlangen, Germany, in 1996 and 2001, respectively.

From 1992 to 1996, he was a Research Assistant with the Telecommunications Institute, University of Erlangen-Nürnberg. In 1997, he was with the IBM Research Laboratory, Zürich, Switzerland. In 1998, he returned to the University of Erlangen-Nürnberg, and in 2005, he spent a sabbatical with ETH Zürich, Zürich. Since 2011, he has been a Full Professor with the University of Ulm, Ulm, Germany. He is currently teaching the undergraduate and graduate courses on signals and systems and digital communications. He authored the textbook *Precoding and Signal Shaping for Digital Transmission* (Wiley, 2002). His current research interests include fast, reliable, and secure digital transmission including single-carrier and multicarrier modulation techniques, information theory, coded modulation, digital communications, signal processing, and especially precoding and shaping techniques.

Dr. Fischer was a recipient of the Dissertation Award from the Technische Fakultät, University of Erlangen-Nürnberg, in 1997, the Publication Award of the German Society of Information Techniques in 2000, the Wolfgang Finkelnburg Habilitation Award in 2002, and the Philipp-Reis-Preis in 2005.